Nanoscale

ROYAL SOCIETY OF CHEMISTRY

PAPER

View Article Online
View Journal | View Issue

Cite this: *Nanoscale*, 2016, **8**, 8236

Open Access Article. Published on 21 March 2016. Downloaded on 23/04/2016 14:47:24.
This article is licensed under a Creative Commons Attribution 3.0 Unported Licence.

Selective modification of nanoparticle arrays by laser-induced self assembly (MONA-LISA): putting control into bottom-up plasmonic nanostructuring†

Nikolaos Kalfagiannis,*[a] Anastasios Siozios,[b] Dimitris V. Bellas,[b] Dimosthenis Toliopoulos,[b] Leon Bowen,[c] Nikolaos Pliatsikas,[d] Wayne M. Cranton,[a,e] Constantinos Kosmidis,[f] Demosthenes C. Koutsogeorgis,[a] Elefterios Lidorikis[b] and Panos Patsalas[d]

Received 24th December 2015,
Accepted 18th March 2016

DOI: 10.1039/c5nr09192f

www.rsc.org/nanoscale

Nano-structuring of metals is one of the greatest challenges for the future of plasmonic and photonic devices. Such a technological challenge calls for the development of ultra-fast, high-throughput and low-cost fabrication techniques. Laser processing, accounts for the aforementioned properties, representing an unrivalled tool towards the anticipated arrival of modules based in metallic nanostructures, with an extra advantage: the ease of scalability. In the present work we take advantage of the ability to tune the laser wavelength to either match the absorption spectral profile of the metal or to be resonant with the plasma oscillation frequency, and demonstrate the utilization of different optical absorption mechanisms that are size-selective and enable the fabrication of pre-determined patterns of metal nanostructures. Thus, we overcome the greatest challenge of Laser Induced Self Assembly by combining simultaneously large-scale character with atomic-scale precision. The proposed process can serve as a platform that will stimulate further progress towards the engineering of plasmonic devices.

Introduction

Nanomaterial and nanodevice manufacturing has traditionally followed two distinct routes: the top-down approach,[1–3] where physical processes such as e-beam and photo-lithography are exploited for slicing and dicing macroscopic entities in the nanoscale, and the bottom-up approach, where atomic-scale chemical forces take centre stage and drive molecular self-assembly.[4–7] Crudely speaking, one might say they correspond to the competing worlds of Physics and Chemistry. In practice, the top-down route offers unparalleled control and reproducibility down to a few nanometres in feature size but at high cost for large area processing, while the bottom-up approach naturally applies for macroscopic scale nano-patterning albeit without the fine feature and reproducibility control. Laser Annealing (LA from now on) might be viewed as the means to a third, intermediate route for nanotechnology manufacturing. Light-matter interactions offer precise energy delivery and control over the physico-chemical processes in the nanoworld. It has already been implemented for the reshaping of plasmonic nanoparticles,[8–11] alloying at the nanoscale[12] and nanomanipulation in optical tweezers.[13–15] Today's laser technology in nano-manufacturing, however, lacks the simultaneous atomic-scale control and large-scale character: processes can be either extremely accurate but implemented in infinitesimally small volumes[8,13] or can be macroscopically implemented with a lesser control on the produced features.[10] In this work we show that it is possible to overcome these limitations and substantially improve the control of bottom-up nano-patterning. The targeted plasmonic applications span from size- and shape-selective biocompatible surfaces,[16] surface enhanced Raman scattering,[17,18] optical storage of information,[10] production of metal nanocavities for light

[a]*Nottingham Trent University, School of Science and Technology, Nottingham, NG11 8NS, UK*
[b]*University of Ioannina, Department of Materials Science and Engineering, 45110 Ioannina, Greece*
[c]*University of Durham, G. J. Russell Microscopy Facility, South Road, Durham, DH1 3LE, UK*
[d]*Aristotle University of Thessaloniki, Department of Physics, 54124 Thessaloniki, Greece*
[e]*Sheffield Hallam University, Materials and Engineering Research Institute, Sheffield, S11 WB, UK*
[f]*University of Ioannina, Department of Physics, 45110 Ioannina, Greece*

† Electronic supplementary information (ESI) available: Extensive experimental results that corroborate the results and conclusions presented in the manuscript, but due to their extent cannot fit in the manuscript. The manuscript refers to specific sections here, but in its entirety this document presents the complete results of our MONA-LISA work. See DOI: 10.1039/c5nr09192f

This journal is © The Royal Society of Chemistry 2016

manipulation and enhancement of solid state lighting,[19,20] as well as broadband solar energy harvesting by incorporating the considered plasmonic nanoparticles into photothermal, photocatalytic and photovoltaic devices.[21–24] At the very heart of these applications lie the light-matter interactions, in the form of coherent surface plasmon oscillations excited by the incident light at specific frequencies with high selectivity on the metal nanostructure's size and shape. But selective plasmon excitation translates into selective light absorption, and thus into selective heating of the nanostructure.

It is natural thus to allow this core property of the target application, to become itself one of the drivers in the self-assembly process. Furthermore, besides heating, selective cooling is also an integral part of restructuring. But as the cooling rate depends on the geometric features of the nanostructure, a second driver for the self-assembly process is introduced.

The available light absorption mechanisms in the case of nanostructured noble metals such as Ag, Au and Cu, can be intuitively summarized in the following modes:

(a) interband absorption, probing the metal's internal d-electrons (Fig. 1a). This is typically enabled at UV frequencies and in general is not size-dependent,

(b) off-resonance intraband (free electron) absorption (Fig. 1b), which however is too weak to cause substantial temperature rise,

(c) resonant intraband absorption (Fig. 1c), probing the conduction electrons with laser wavelengths close to the spectral position of Localised Surface Plasmon Resonance (LSPR). This mechanism is strongly size- and shape-selective, and

(d) photon ionization that may occur only for high laser fluences.[25]

As an example, the overall absorption spectrum of Ag nanoparticle with diameter of 40 nm on top of a Si substrate is plotted in Fig. 1d, showing the spectral domains of the two absorption mechanisms. Hereby, we utilize modes (a) and (c), combined with the size selectivity of cooling (~nanostructure surface/volume ratio) and demonstrate that this approach provides an exceptional and versatile tool for controlling the self-assembly of nanoparticles, leading to desired nanoparticles distributions, which cannot be achieved by the exclusive use of UV laser annealing.

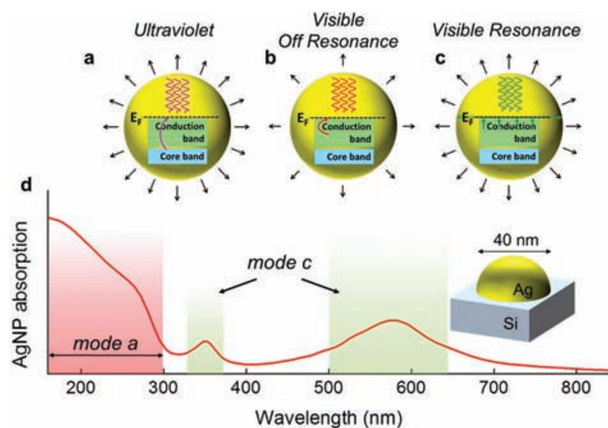

Fig. 1 (a–c) Schematic representation of the main physical mechanisms of absorption we exploit in the current work and their corresponding thermal effect on metallic nanostructures. (d) Calculated absorption spectrum of a 40 nm diameter Ag nanoparticle (Ag NP) on top of a Si substrate, as shown in the inset schematic. Interband absorption (mode a) dominates the red shaded region, while intraband absorpiton (LSPR driven, mode c) is dominating the green shaded regions (at ~350 nm the quadrupole and ~580 nm the dipole LSPR contributions respectively).

Open Access Article. Published on 21 March 2016. Downloaded on 23/04/2016 14:47:24.
This article is licensed under a Creative Commons Attribution 3.0 Unported Licence.

Experimental

Sample preparation

Metallic thin films were deposited employing the following experimental techniques:

- Radio-Frequency Magnetron Sputtering in a high vacuum chamber (base pressure <10^{-3} Pa, Ar pressure 0.67 Pa, 3″ Ag or Cu or Au targets 99.99%, power at the target set at 40 W, 11 rpm substrate rotation) on commercial, Czochralski-grown, n-type (resistivity 1–10 Ω cm) Si(100) wafers, with a 2 nm native oxide. The deposition time varied in order to get thin films of an effective thickness of 5 and 10 nm. These substrates served as core templates in the framework of the present study.

- Electron Beam Evaporation in an ultra-high vacuum chamber (base pressure <10^{-6} Pa). The e-gun was operated at 6 V and 50 mA. Ag thin films of an effective thickness of 10 nm were produced on commercial n-type Si(100) wafers.

- Chemical reduction of $AgNO_3$ on commercial n-type Si (100) wafers by drop casting a droplet (30 μl) of a solution containing 0.001 M $AgNO_3$ and 0.01 M HF was casted on to Si at room temperature in ambient environment for 10 min. The samples were rinsed with HPLC grade water and dried in air flow.

Sample processing

Laser Annealing (LA) was carried out with an Excimer laser (LAMBDA PHYSIK LPX 305i) which is capable of delivering unpolarized light (pulse length of 25 ns) and up to 1200 mJ per pulse at 248 nm (KrF) and 600 mJ per pulse at 193 nm (ArF). The raw beam is approximately 30 mm × 15 mm with a Gaussian like profile on the long axis and an almost top-hat profile on the short axis. The beam delivery system comprises a variable attenuator, a beam homogeniser and a mask-projection system. A X–Y–Z translational stage was used in order to manipulate the sample during the laser process. The laser spot delivered onto the samples was set, by an appropriate mask, to be a 2.5 × 2.5 mm^2 spot. An extensive experimental schedule was followed, varying the number of pulses (1 to 15 at 1 Hz repetition rate) and the fluence (200–900 mJ cm^{-2} with a step of 50 mJ cm^{-2}).

Selected samples, with LSPR close to 532 nm, were irradiated with laser pulses generated by the second harmonic of a Nd:YAG laser (pulse width of 6 ns). Samples with LSPR close to 620 nm were irradiated with laser pulses generated by an Optical Parametric Oscillator (OPO) unit pumped by the third harmonic (355 nm) of the Nd:YAG. The fluence ranged from 75–175 mJ cm^{-2} and the repetition rate was set at 10 Hz.

Open Access Article. Published on 21 March 2016. Downloaded on 23/04/2016 14:47:24. This article is licensed under a Creative Commons Attribution 3.0 Unported Licence.

Sample characterisation

Samples were imaged by Scanning Electron Microscopy (SEM) in Plan-View (Top Down) using a FEI Helios Nano lab 600 MK2. High-End imaging was obtained with an ultra-short working distance of 2.4 mm and an operating voltage of 3 keV. The High-End operating mode utilised the "Through Lens Detector" in immersion mode. SEM images were analysed with an open source software (imageJ) to acquire statistical information on the nanoparticle's size distribution in relation to the surface coverage of the nanoparticles (ratio of the footprint area covered by the particles to the total area).

The optical properties of the samples were studied on a home-built spectroscopic reflectivity measurement system (200–870 nm range) at normal incidence using a white light deuterium-halogen source (Ocean Optics DH-2000), a co-axial fiber-optic assembly (Avantes reflection probe), a high line density grating and a CCD detector (Ocean Optics USB4000); the reflectivity spectra were normalized using a silicon reference mirror.

Optical and thermal calculations

A full-vector 3D finite-difference time-domain (FDTD) simulator[26,27] for Maxwell's equations[28] with a narrow Gaussian-temporal-profile plane-wave normal incidence was used, where the detailed spatial absorption distribution $\alpha(z)$ was extracted for each frequency by Fourier transformations.[29] Material dielectric properties were taken from literature.[30] The plasmonic structure studied was a hexagonal array of hemispherical Ag domes at separation/diameter = 1.2 ratio.

Due to the extended pulse profile (~millimeters) and shallow heating depth (~microns), solving the 1D heat diffusion equation[31] suffices, where a variable area $s(z)$ was assumed as a function of depth z in order to take into account the actual shape of the nanoparticles:

$$s(z)c(z)\rho(z)\frac{\partial T(z,t)}{\partial t} = \frac{\partial}{\partial z}\left[s(z)k(z)\frac{\partial T(z,t)}{\partial z}\right] + s(z)Q(z,t) \quad (1)$$

Material parameters (heat capacity $c(z)$, mass density $\rho(z)$ and thermal conductivity $k(z)$) were taken from literature.[32]

An extended laser heating source term $Q(z,T) = \alpha(z)\cdot\phi(t)$ was used, defined by the product of the absorption spatial profile $\alpha(z)$ (obtained from the FDTD calculations) and the experimental laser pulse temporal profile $\varphi(t)$ (either that of an excimer or of a Nd:YAG laser depending of laser annealing wavelength assumed), where the total laser fluence was:

$$\Phi = \int_{-\infty}^{\infty} \phi(t)\mathrm{d}t \quad (2)$$

Upon time-integration of the heat diffusion equation we derived the temperature transient profile at every point in the structure. We assumed that (i) electronic and lattice temperatures were in equilibrium (valid for slow heating times in the ns regime[33]) and (ii) radiation and convection losses were insignificant (indeed, even for a temperature of about 5000 K, unit emissivity and forced air cooling for the duration of the laser annealing pulse (~30 ns), we found radiation and convection losses of the order of 0.1 mJ cm^{-2}, which were many orders of magnitude smaller than the typical fluence used in this study). Furthermore, since we were only interested in estimating the temperature rise and not in the exact physics at the very high temperatures, we simplified our calculations by (iii) assuming that the material properties (absorption, heat capacity, mass density and thermal conductivity) remained constant during heating and by (iv) ignoring the thermodynamics of phase changes, *e.g.* melting and resolidification.

Results and discussion

Theoretical investigation

Computer simulations can help us explore the potential use of the various modes presented above. Assume for example that after some laser treatment of a Ag thin film, an array of 40 nm in diameter hemispherical nanoparticles (Ag NP) has been formed within some area on top of a Si substrate. We first consider what the effect of a new incoming laser pulse would be. In Fig. 2a the absorption per nm is plotted at different depths for this structure.

The different modes relating to interband and intraband absorptions in the nanoparticle, as well as the absorption in the substrate, are clearly shown. These kinds of detailed absorption distribution maps are a necessary input in the thermal dissipation calculations. As a particular case, assume the UV 248 nm and VIS 532 nm wavelengths, corresponding to the KrF excimer and the 2nd harmonic of the Nd:YAG lasers respectively, used in our experimental demonstrations. These are indicated by the dashed lines in Fig. 2a and their corresponding absorption profiles are plotted in detail in Fig. 2b. Furthermore, the actual laser pulse profiles are shown in Fig. 2c. Combining these two in the heat dissipation equation (eqn (1)), we solve for the transient temperatures developed in the nanoparticles, plotted in Fig. 2d. For simplicity, we have assumed a linear response regime and plot the temperature rise per laser fluence (in mJ cm^{-2}). We note here that the temperature transient follows the actual pulse temporal shape, but a significant transient tail also persists for longer times. These two features indicate that the processes studied here are both power and fluence dependent respectively, making the explicit time-dependent simulations necessary. For a particular laser fluence, direct information regarding particle heating is extracted, and the probability of the nanoparticle melting or not can be assessed.

The global picture is then constructed by considering how nanoparticle arrays of different sizes of nanoparticles react to different wavelength illuminations, which is plotted in Fig. 2e, showing the peak transient temperature developed (per unit of laser fluence) in the nanoparticle as a function of wavelength and nanoparticle size. Note that the apparent "band" at around 500 nm (Fig. 2e, right panel) is the continuation of the previous panel, as evident by the scale bars. Indeed, the dipole contribution is weaker than the contributions at shorter wave-

 This journal is © The Royal Society of Chemistry 2016

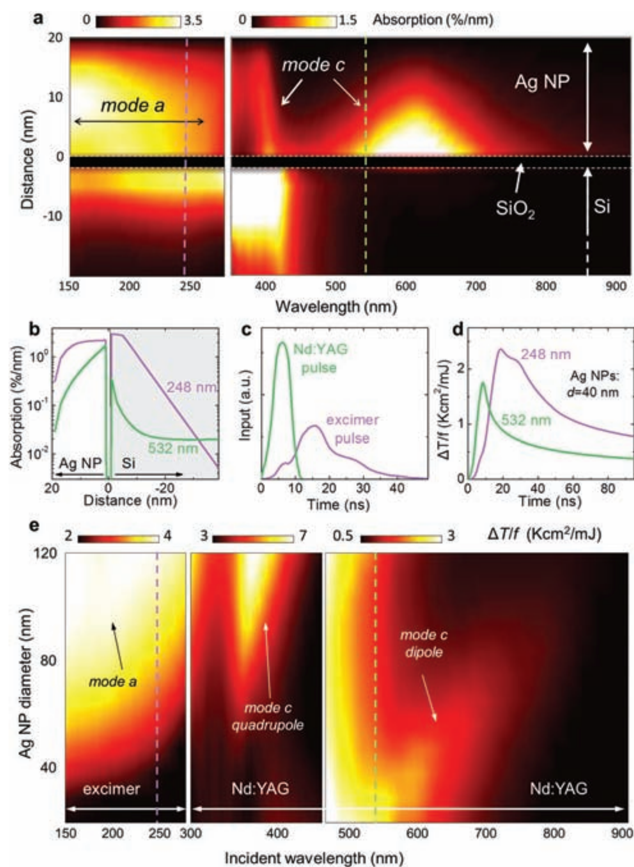

Fig. 2 (a) Calculated vertical absorption profile for the 40 nm diameter Ag nanoparticle in units of percent per nanometer. Indicated with the two dashed lines are the two primary wavelengths used in this study. (b) Absorption percentage per nm profile in our model structure for the two principal wavelengths used in the study. (c) Measured temporal profile of the two laser sources used. (d) Corresponding temperature transients developed in the Ag NP, normalized to the laser fluence. (e) Calculated global map showing the peak temperature developed in a Ag NP on top of Si as a function of laser wavelength and NP size. The dashed lines indicate the two primary wavelengths used in this study.

lengths (combined quadrupole LSPR and bulk Si absorption), however, within our proposed selective annealing scheme we always irradiate at a single wavelength, and so the relative strength of each band is of no importance other than defining the laser fluence that should be used in each case.

The size dependence of the different absorption mechanisms is now fully revealed: interband transitions (mode a) and quadrupole LSPR (mode c) favour the melting of the larger nanoparticles, while the dipole LSPR (mode c) favors the melting of the smaller nanoparticles. It is important to note here that for mode (c) the peak absorption is generally redshifted from the actual LSPR frequency (at which a maximum in reflectivity is found), with increasing redshift for larger nanoparticles. Upon resolidification, a random distribution of sizes will emerge. However, a repeated laser treatment at a particular wavelength will lead to the repeated melting of one particular size group and thus to its eventual extinction. This is the main concept behind our approach: repeated laser treatments, targeting different nanoparticle size groups with different laser wavelengths, driving the final size distribution towards the predetermined one. We call this process: 'Modification of Nanoparticles Arrays by Laser-Induced Self Assembly' (MONA-LISA).

Experimental investigation

We now proceed to the experimental demonstration of MONA-LISA. Our first step is a single shot UV LA to initialize nanoparticle formation from a semi-continuous metal thin film, by Laser Induced Self-Assembly (LISA). This results to the restructuring of noble metal (Cu, Ag, Au) layers into nanoparticle arrangements in macroscopic scales (several mm^2 and with potential for substantial upscaling).

This LISA process with a UV laser (248 nm) is strongly fluence-dependent as demonstrated in the SEM images of Fig. 3a(i, iii, v, vii). The "as grown" sample is also shown in Fig. 3a(ix) for comparison. The Ag NP size distributions are generally bimodal, consisting of one set of coarse and one set of fine nanoparticles (NP). Increasing the laser fluence from 350 mJ cm^{-2} to 800 mJ cm^{-2} results in a decreasing difference between the two NP sets, as shown by the quantified SEM images (Fig. 3b, purple, cyan, yellow and red bars). The bimodal NP size distributions are accompanied by two corresponding LSPR peaks in the optical reflectivity spectra (Fig. 3c, purple, cyan, yellow and red lines). The coarse particles are

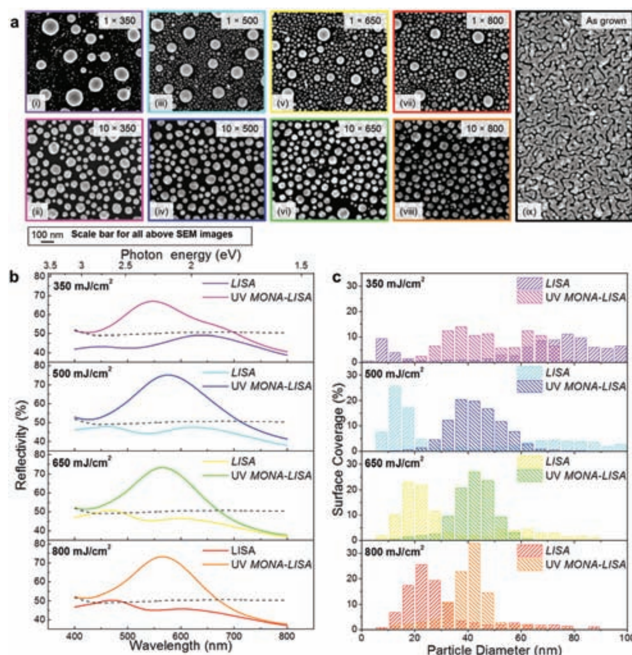

Fig. 3 (a) SEM images of samples processed with LISA (1 pulse, 248 nm LA) and UV MONA-LISA (10 pulses, 248 nm) under various applied fluences (i–viii), including the as grown sample (ix). (b) The effect of LISA and UV MONA-LISA on the optical reflectivity spectra of a 10 nm Ag thin film under various applied fluences. The spectra of the as grown is shown with a dashed line for comparison. (c) Surface coverage of the nanoparticles in relation to the particle diameter for all the cases of (a).

Open Access Article. Published on 21 March 2016. Downloaded on 23/04/2016 14:47:24.
This article is licensed under a Creative Commons Attribution 3.0 Unported Licence.

Open Access Article. Published on 21 March 2016. Downloaded on 23/04/2016 14:47:24.
This article is licensed under a Creative Commons Attribution 3.0 Unported Licence.

accompanied by a region of depleted Ag around them, indicating that they are formed in the expense of the fine particles *via* surface diffusion and an Ostwald ripening process. At higher fluence the Ostwald ripening process becomes less pronounced and results into a higher population of fine particles and a smaller size of the coarse particles. This behaviour indicates that the process is more thermal for lower fluence, which superficially contradicts the simplified thermal description. In fact, the higher fluence is sufficient to produce hot electrons during the pulse,[25] resulting into ionization and positive charging of Ag nanoparticles. This hinders the Ostwald ripening process *via* Coulomb repulsion among the nanoparticles and stabilizes them in well separated distances. This argument is further supported by considering the results of the LISA process with a 193 nm laser (see the ESI, section 1.2, page 5, Fig. S4†). Indeed, for the 193 nm UV LA the bimodal distribution is less pronounced, even for the lower fluence, due to the higher ionization probability of Ag when irradiated by higher energy photons. On the contrary, LISA is not possible at all for long wavelengths, *e.g.* the 532 nm used in this work, due to the high reflectivity of metallic layers at these wavelengths.

The modification of nanoparticle assemblies by multiple laser pulses (MONA-LISA process) involves quite different physics due to the selective optical absorption and heat dissipation by the nanoparticles, as mentioned earlier. In order to demonstrate this, we subject the initial assemblies of nanoparticles produced by LISA to a series of UV and/or VIS LA steps. We explore this process with the laser wavelengths 193, 248, 532 and 620 nm and combinations of them for a variety of fluences, number of sequential pulses and initial metal film thickness of 5 and 10 nm for Ag on a Si(100) substrate. Furthermore we investigate the process for Au and Cu thin films, deposited *via* sputtering (for more details refer to the ESI,† sections 1.3–1.4, page 6). Additionally, we demonstrate that our proposed process is independent to the thin film fabrication technique by applying MONA-LISA to Ag film deposited by e-beam evaporation as well as chemical reduction of $AgNO_3$ (for more details refer to the ,† section 2.1.ii: page 34).

First we consider the case of UV MONA-LISA, *i.e.* processing by multiple UV (248 nm) laser pulses, and we correlate the effect of interband absorption with the size-selective heat dissipation; Fig. 3c shows the optical reflectivity spectra of a 10 nm Ag film recorded after UV MONA-LISA using 10 successive UV laser pulses at various fluences (magenta, blue, green and orange lines for 350, 500, 650, 800 mJ cm^{-2}, respectively). Comparing these spectra with those for the previous LISA processing (purple, cyan, yellow and red lines) reveals that the consecutive pulses transform the two reflectivity peaks to one, indicating a gradual transformation of the bimodal distributions to unimodal (reflectance data for intermediate cases of less than ten successive pulses are presented in the ESI, section 1.2: Fig. S4,† page 5). This is also confirmed by the corresponding SEM images in Fig. 3a(ii, iv, vi, viii) and the size distribution histograms in Fig. 3b (magenta, blue, green and orange bars), respectively. The reshaping of the particles is a combination of the disappearance of the coarse particles (by melting upon LA) and the enlargement of the surrounding fine particles, as they become the recipients of mass transfer from the melted coarse ones.

The physics behind that observation is based on the faster heat dissipation from the finer nanoparticles due to their higher effective surface (surface to volume ratio). As a result, the finer nanoparticles remain cold during UV MONA-LISA. This was quantified by photothermal calculations, which determine the equi-temperature contour lines *vs.* nanoparticle diameter, from which the critical size under which every particle remains practically cold during the UV MONA-LISA process of Ag on Si can be inferred; assuming for simplicity the bulk Ag melting temperature of 960 °C, the calculated values of the critical diameter *vs.* the fluence of the 248 nm laser are presented in Fig. 4a. Note that the critical diameter is strongly dependent on the thermal conductivity of the substrate, as a less thermally conductive substrate would hinder

Fig. 4 (a) Critical nanoparticle diameter (the diameter value under which every particle remains practically cold during the UV LA process; hence these particles cannot be further manipulated upon irradiation) as a function of applied laser fluence. The inset shows an optical microscopy image of the "Marie Curie Actions" logo produced by projection mask under LISA/UV MONA-LISA. Each colour represents a different UV LA fluence. (b) A digital photo of a grid of LISA/UV MONA-LISA spots (2.5 × 2.5 mm^2 each) of varying fluence (*x*-axis) and number of pulses (*y*-axis) produced on a 10 nm Ag thin film. (c) Contour plot of the dominant LSPR maximum acquired from optical reflectivity spectra from each spot of (b) (in the case of bimodal responses, the spectral value of the stronger reflectivity peak is reported).

heat dissipation.[34] For example, SiC should behave very similarly to Si, having similar thermal conductivities (Si: 150 W m^{-1} K^{-1}, SiC: 140–180 W m^{-1} K^{-1}). The behaviour of MgO and Al_2O_3 should also be similar as well, albeit would require lower fluences to achieve similar nanoparticle arrangements due to their lower thermal conductivity (Al_2O_3: 25–30 W m^{-1} K^{-1}, MgO: 45–60 W m^{-1} K^{-1}). SiO_2 on the other hand is thermally resistive enough (SiO_2: 1.5–2 W m^{-1} K^{-1}) to probably change the process, *i.e.* the heating and cooling rates would be much smaller, and so the particle shaping should be quite different.

The UV MONA-LISA process is thus based on the larger particles having the ability to raise their temperature above their melting point, and consequently melting and re-solidifying forming smaller particles with a stochastic size distribution, while the smaller ones remain below the melting threshold and therefore remain practically unaffected. Evidently, successive pulses suppress the population of the coarse particles, gradually transforming them to stable finer particles *via* stochastic size redistribution.

A secondary mechanism is observed as the laser fluence is increased to high values; in particular, above 700 mJ cm^{-2} a gradual decrease in the absolute reflectivity values is observed when several pulses are used (see ESI, section 1.1: Fig. S3,† page 4) indicating loss of material due to ablation, concomitantly with a slight blueshift of the LSPR peak (due to increased empty space between the nanoparticles). This mechanism is also observed for high fluence UV MONA-LISA processing at other wavelengths, such as the 193 nm (see ESI, section 1.1: Fig. S2, page 3 and section 1.2: Fig. S4,† page 5), and 355 nm (studied and reported by Stietz *et al.*[35]). In fact, ablation is observed at a lower fluence (650 mJ cm^{-2}) for the 193 nm laser, due to the higher energy of the corresponding photons.

The wide range of size distributions achieved by LISA and UV MONA-LISA results in a vast colour palette as those presented in Fig. 4b and c (real colour appearance of the Ag nanoparticle assemblies and quantitative spectral reflectivity response, respectively), which quantifies UV MONA-LISA as a process most capable for tuning the size and distribution of NPs and thus their plasmonic resonance wavelength, spanning from 480–735 nm as shown in Fig. 4c. Combining the LISA and MONA-LISA process with projection masks may produce multicolour images of high spatial resolution and colour contrast as that presented in the inset of Fig. 4a, depicting the logo of the "Marie Curie Actions" (People Programme – EU:FP7).

The implementation of MONA-LISA employing exclusively UV pulses has the inherent limitation of not being able to probe nanoparticles of size below the critical size described in Fig. 4a. This has the severe consequence that only the coarse particles are affected after successive laser pulses. In order to directly probe and manipulate the finer particles we must exploit their selective optical absorption *via* LSPR using a visible laser wavelength that would result in stronger optical absorption and hence higher temperature rise, as predicted by the computational results presented in Fig. 2e.

The optimum condition for narrowing the bandwidth of the LSPR at 532 nm was achieved by applying 500 pulses at 125 mJ cm^{-2} (refer to ESI, section 2.1: Fig. S7,† page 7). The fact that hundreds of VIS pulses are needed in order to induce a change reflects the lower temperature rise profile per pulse (compared to the UV processing where 10 pulses are enough to reach a steady state), as predicted by the computational results of Fig. 2e, where a lower temperature rise is evident at VIS wavelengths compared to UV processing.

Nevertheless, this combined process produces plasmonic nanoparticle assemblies with size distributions comparable to colloidal nanoparticles,[17,36] but crucially with our MONA-LISA method they are firmly attached on the substrate.

A broader view of the VIS MONA-LISA process, that demonstrates its selective nature, is obtained by considering its effect to Ag nanoparticle assemblies of varying size distributions. For this purpose we compare two grids of samples pre-processed by LISA and subsequently processed by VIS MONA-LISA and UV MONA-LISA (Fig. 5a, left-hand side and right-hand side, respectively). Each grid consists of square spots (2.5 ×

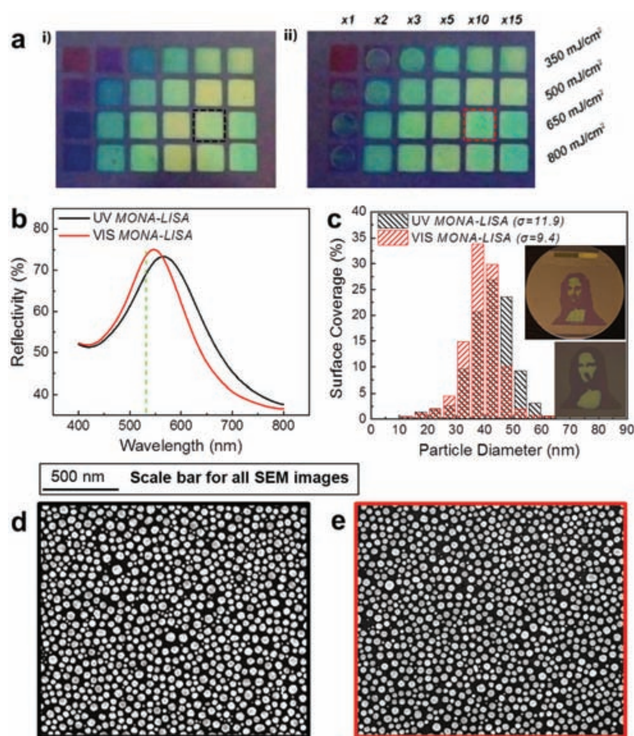

Fig. 5 (a) A digital photo of a grid of LA spots of varying fluence (*y*-axis) and number of pulses (*x*-axis) produced on a 10 nm Ag thin film: (i) produced *via* the LISA/UV MONA-LISA process and (ii) replica of (i) with subsequent VIS MONA-LISA treatment (combined UV and VIS laser annealing). (b) Optical response of a Ag/Si sample (initial effective thickness of 10 nm) after UV MONA-LISA (10 pulses, 248 nm at 650 mJ cm^{-2} – black line) and UV+VIS MONA-LISA (10 pulses, 248 nm at 650 mJ cm^{-2} and 500 pulses, 532 nm at 125 mJ cm^{-2} – red line). (c) Surface coverage of the nanoparticles in relation to the particle diameter for the two spots indicated with red and black dashed boxes in (a) and with optical response shown in (b). Inset depicts two portraits of Da Vinci's Mona Lisa validating the potential and scalability of the MONA-LISA process. (d) SEM image of the UV MONA-LISA sample. (e) SEM image of the UV+VIS MONA-LISA sample.

Open Access Article. Published on 21 March 2016. Downloaded on 23/04/2016 14:47:24.
This article is licensed under a Creative Commons Attribution 3.0 Unported Licence.

2.5 mm^2) pre-processed by 1, 2, 3, 5, 10 and 15 pulses of 248 nm at fluences of 350, 500, 650, 800 mJ cm^{-2}. All spots on the left-hand side grid only were subsequently processed by VIS MONA-LISA with 500 pulses from a 532 nm laser (2nd harmonic from an Nd:YAG laser) at 125 mJ cm^{-2} (round laser spot of 2 mm in diameter). After applying VIS MONA-LISA there is a remarkable change in their optical response. This is vividly illustrated in the left-hand side grid of Fig. 5a where the circular Nd:YAG spot (the result of VIS MONA-LISA) is clearly distinguished inside the excimer pre-treated square (the result of the UV LISA). The appearance of all VIS MONA-LISA spots shifts to green proving the reshaping of the nanoparticles to sizes that exhibit LSPR at the processing wavelength. In particular, if we consider the two spots indicated in Fig. 5a with a black and a red dashed box, the shift to green after VIS MONA-LISA is depicted in their optical reflectance spectroscopy data shown in Fig. 5b. Fig. 5c shows their particle size distributions, as calculated from image analysis of their corresponding SEM images (Fig. 5d and e), where it is clearly evident that the VIS MONA-LISA process creates a narrower size distribution around 40 nm diameter. This is also evident by the decrease of the standard deviation (σ) values (expressed in nm), which the VIS MONA-LISA process demonstrates. The values of σ are shown in Fig. 5c and present a measure of the variability of the size distribution of the nanoparticle array for each sample. Nanoparticles with LSPR close to the processing wavelength (532 nm) are less affected by the laser process due to their high reflectivity in that particular wavelength. The melting process requires a high temperature, which scales with the total absorption of the system. At the LSPR frequency the reflectivity becomes maximum and thus the total system absorption becomes minimum. However the rest of the particles melt and upon re-solidification some of those will eventually cool down to a size that is giving a resonance close to 532 nm. These nanoparticles will remain now practically cold and as this process evolves, the majority of the particles that prevail will be of that particular size.

This effect of VIS MONA-LISA is more pronounced in the cases of nanoparticle assemblies with optical response away from green: for example all the LISA pre-treated spots (first column in grid of Fig. 5a). Examining the later in more detail one can see that the LSPR created by the initial UV MONA-LISA process (248 nm, 2 × 350 mJ cm^{-2}) exhibits a double reflectance peak, due to its bimodal nanostructuring, notably with no particular response close to 532 nm, as shown in Fig. 6a (black line, UV MONA-LISA). Applying VIS MONA-LISA to this area, with 500 pulses (i), 2000 pulses (ii) and 4000 pulses (iii) results in gradually changing the bimodal distribution to one with a peak very close to the processing wavelength (532 nm). Their nanoparticle distributions are presented in the histograms of Fig. 6b, as resulted from the corresponding SEM images shown in Fig. 6c–f. It is noteworthy that the VIS MONA-LISA probes particularly the finer Ag nanoparticles (<20 nm), confirming the computational analysis presented in Fig. 2e. Similar behaviour was observed using other visible wavelengths. For example, applying VIS MONA-LISA at 620 nm onto

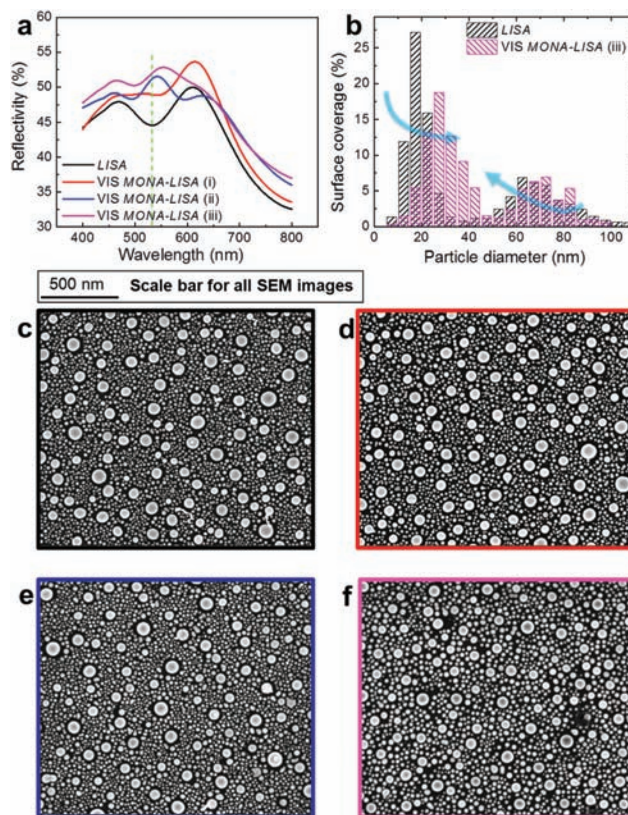

Fig. 6 (a) Optical reflectivity spectra of UV MONA-LISA (2 pulses, 248 nm at 350 mJ cm^{-2} – black line), used as a template for the subsequent VIS MONA-LISA (532 nm at 125 mJ cm^{-2}) with 500 pulses (red line), 2000 pulses (blue line) and 4000 pulses (magenta line). The green dashed line sets the 532 nm mark. (b) Surface coverage of the nanoparticles in relation to the particle diameter for all the cases of (a). (c) SEM image of the UV MONA-LISA processed sample. (d) SEM image of the VIS MONA-LISA (i) sample (500 pulses). (e) SEM image of the VIS MONA-LISA (ii) sample (2000 pulses) and (f) SEM image of the VIS MONA-LISA (iii) sample (4000 pulses).

the above mentioned UV MONA-LISA sample produced by 248 nm with 2 × 350 mJ cm^{-2}, results in a shift of the LSPR peak from ∼650 nm to ∼625 nm (refer to the ESI, section 2.3, Fig. S38,† page 35). This proves the general character of the VIS MONA-LISA approach and the flexibility of producing any selected plasmonic particle distribution by probing their LSPR absorption during visible laser annealing.

From the practical point of view, combining the two laser wavelengths (UV and VIS) and appropriately selecting the processing conditions (number of pulses and fluence), provides an unprecedented asset for tuning the nanoparticle assemblies into size distributions that are:

(i) Bimodal (UV LISA),

(ii) Multimodal (UV LISA and VIS MONA-LISA of intermediate number of pulses),

(iii) Unimodal of a limited variation in size due to self-assembly and heat dissipation selectivity (UV MONA-LISA),

(iv) Unimodal of any size due to LSPR selectivity (UV MONA-LISA and VIS MONA-LISA at steady state).

Open Access Article. Published on 21 March 2016. Downloaded on 23/04/2016 14:47:24.
This article is licensed under a Creative Commons Attribution 3.0 Unported Licence.

Open Access Article. Published on 21 March 2016. Downloaded on 23/04/2016 14:47:24. This article is licensed under a Creative Commons Attribution 3.0 Unported Licence.

The last case (iv) goes beyond any laser-driven process for particle formation reported so far, and provides enhanced control and selectivity on the particle formation, allowing us to drive them towards narrower distributions. At the same time, besides unimodal distributions the MONA-LISA process can also be tuned to produce multimodal distributions with broadband optical response covering the entire visible range, which is of particular importance for example in solar harvesting applications.

The potential and scalability of the MONA-LISA process is finally demonstrated by the two portraits of Da Vinci's "Mona Lisa" presented as insets in Fig. 5c. The upper inset is a macroscopic, large-scale pattern created with two contact masks on a 2″ Si wafer coated with 10 nm Ag (purple areas correspond to a process of one pulse at 500 mJ cm^{-2}, whereas the green areas to three pulses of the same fluence). It was realized by rastering the UV laser annealing with a pixel size of 2.5 × 2.5 mm^2. On the contrary, the lower inset is a microscopic pattern (2.5 × 2.5 mm^2) created on the same wafer in a single pixel processing using two projection masks. The resolution of the method may be further reduced to a feature size less than a micron (restricted only by the diffraction limit and taking into account that in this case we would need a 3D model to simulate the process) by using appropriate photolithographic or projection masks.[10]

The UV MONA-LISA process has been also tested in Au and Cu thin films (shown in the ESI, section 1.3, 1.4, Fig. S5, S6† respectively, page 6). The results show that NP formation is possible albeit the successful processing window becomes narrower. Especially for Cu's case, its LSPR is too deep into the red-IR range and the LSPR strength is more faint than that of Ag and Au, therefore the VIS MONA-LISA is not expected to be as effective.

Conclusions

Different optical absorption and heat diffusion mechanisms in plasmonic metal nanoparticles were taken into advantage as a means of controlling matter at the nanoscale, *via* laser driven processes for restructuring a metal thin film into a predetermined nanoparticle template.

The stochastic recrystallization of melted metal nanoparticles by UV processing only is governed by the morphology of the particle template itself, *i.e.* the existence of a critical size diameter as a function of the laser fluence. This self-limiting process (that in some cases may well provide the desired outcome) could be overcome by the subsequent application of VIS processing, allowing a further modification to the nanoparticles templates. This is due to the selective heat dissipation from the nanoparticle size groups away from the VIS processing laser wavelength, providing an exceptional capability for selective formation of nanoparticles with predesigned and desired size distributions. As a result, successive pulses of UV LA reduce the volume fraction of larger nanoparticles (>50 nm), while VIS LA may either further refine the size distributions or induce the emergence of nanoparticles, which exhibit LSPR close to the irradiation wavelength. This combined UV and VIS LA treatment provides unprecedented control on the size distributions and plasmonic behaviour of nanoparticle arrays of noble metals (Ag, Au, Cu), independently of their deposition method and can create nanoparticles with sizes and distributions that are otherwise impossible to produce by single wavelength UV laser annealing. We have named this approach MONA-LISA: Modification of Nanoparticle Arrays by Laser-Induced Self Assembly.

Acknowledgements

N. Kalfagiannis acknowledges funding from People Programme (Marie Curie Actions) LASER-PLASMON of the European Union's Seventh Framework Programme (FP7/2007–2013) under REA grant agreement no. PIEF-GA-2012-330444.

A. Siozios and D. V. Bellas acknowledge funding from the following sources: the European Union (European Social Fund – ESF) and Greek national funds through the Operational Program "Education and Lifelong Learning" of the National Strategic Reference Framework (NSRF) – Research Funding Program: Heracleitus II.

The research activities of P. Patsalas and E. Lidorikis that led to these results were co-financed by Hellenic Funds and by the European Regional Development Fund (ERDF) under the Hellenic National Strategic Reference Framework (NSRF) 2007–2013, according to contract no. 11ΣΥΝ-5-1280 of the Project 'Nano-Hybrid', within the Program 'Competitiveness and Entrepreneurship'.

D. C. Koutsogeorgis acknowledges the School of Science and Technology at Nottingham Trent University for the approval of a sabbatical made possible *via* QR funds, and the Higher Education Funding Council for England (HEFCE) for providing the QR funds as a result of the Research Assessment Exercise 2008 (RAE2008).

The authors would like to acknowledge Dr B. Boudjelida, for providing access to a Dimension FastScan Atomic Force Microscope at BRUKER's headquarter's, Coventry, UK and Dr Robert Ranson for providing training on the Nd:YAG laser used for this work.

Notes and references

1 Z. H. Nie and E. Kumacheva, *Nat. Mater.*, 2008, **7**, 277.
2 E. J. Menke, M. A. Thompson, C. Xiang, L. C. Yang and R. M. Penner, *Nat. Mater.*, 2006, **5**, 914.
3 J. Yang, T. Ling, W. T. Wu, H. Liu, M. R. Gao, C. Ling, L. Li and X. W. Du, *Nat. Commun.*, 2013, **4**, 1695.
4 T. Scheibel, R. Parthasarathy, G. Sawicki, X. M. Lin, H. Jaeger and S. L. Lindquist, *Proc. Natl. Acad. Sci. U. S. A.*, 2003, **100**, 4527.
5 J. Y. Cheng, A. M. Mayes and C. A. Ross, *Nat. Mater.*, 2004, **3**, 823.

Open Access Article. Published on 21 March 2016. Downloaded on 23/04/2016 14:47:24.
This article is licensed under a Creative Commons Attribution 3.0 Unported Licence.

6 W. Lu and C. M. Lieber, *Nat. Mater.*, 2007, **6**, 841.
7 M. W. Li, R. B. Bhiladvala, T. J. Morrow, J. A. Sioss, K. K. Lew, J. M. Redwing, C. D. Keating and T. S. Mayer, *Nat. Nanotechnol.*, 2008, **3**, 88.
8 J. Rongchao, C. YunWei, C. A. Mirkin, K. L. Kelly, G. C. Schatz and J. G. Zheng, *Science*, 2001, **294**, 1901.
9 M. J. Beliatis, N. A. Martin, E. J. Leming, S. R. P. Silva and S. J. Henley, *Langmuir*, 2010, **27**, 1241.
10 A. Siozios, D. C. Koutsogeorgis, E. Lidorikis, G. P. Dimitrakopulos, T. Kehagias, H. Zoubos, P. Komninou, W. M. Cranton, C. Kosmidis and P. Patsalas, *Nano Lett.*, 2012, **12**, 259.
11 A. Stalmashonak, H. Graener and G. Seifert, *Appl. Phys. Lett.*, 2009, **94**, 193111.
12 S. J. Henley, M. J. Beliatis, V. Stolojan and S. R. P. Silva, *Nanoscale*, 2013, **5**, 1054.
13 D. G. Grier, *Nature*, 2003, **424**, 810.
14 J. R. Moffitt, Y. R. Chemla, D. Izhaky and C. Bustamante, *Proc. Natl. Acad. Sci. U. S. A.*, 2006, **103**, 9006.
15 T. L. Gustavson, A. P. Chikkatur, A. E. Leanhardt, A. Gorlitz, S. Gupta, D. E. Pritchard and W. Ketterle, *Phys. Rev. Lett.*, 2002, **88**, 020401.
16 M. Potara, M. Baia, C. Farcau and S. Astilean, *Nanotechnology*, 2012, **23**, 055501.
17 M. J. Mulvihill, X. Y. Ling, J. Henzie and P. D. Yang, *J. Am. Chem. Soc.*, 2010, **132**, 268.
18 N. T. Panagiotopoulos, N. Kalfagiannis, K. C. Vasilopoulos, N. Pliatsikas, S. Kassavetis, G. Vourlias, M. A. Karakassides and P. Patsalas, *Nanotechnology*, 2015, **26**, 205603.
19 V. Giannini, Al. Fernandez-Dominguez, Y. Sonnefraud, T. Roschuk, R. Fernandez-Garcia and S. A. Maier, *Small*, 2010, **6**, 2498.
20 V. Giannini, Al. Fernández-Domínguez, S. C. Heck and S. A. Maier, *Chem. Rev.*, 2011, **111**, 3888.
21 H. Zoubos, L. E. Koutsokeras, D. F. Anagnostopoulos, E. Lidorikis, S. A. Kalogirou, A. R. Wildes, P. C. Kelires and P. Patsalas, *Sol. Energy Mater. Sol. Cells*, 2013, **117**, 350.
22 N. Kalfagiannis, P. G. Karagiannidis, C. Pitsalidis, N. T. Panagiotopoulos, C. Gravalidis, S. Kassavetis, P. Patsalas and S. Logothetidis, *Sol. Energy Mater. Sol. Cells*, 2012, **104**, 165.
23 H. A. Atwater and A. Polman, *Nat. Mater.*, 2010, **9**, 205.
24 F. Pincella, K. Isozaki and K. Miki, *Light: Sci. Appl.*, 2014, **3**, e133.
25 W. Nichols, G. Malyavanatham, D. Henneke, D. O'Brien, M. Becker and J. Keto, *J. Nanopart. Res.*, 2002, **4**, 423.
26 E. Lidorikis, S. Egusa and J. D. Joannopoulos, *J. Appl. Phys.*, 2007, **101**, 054304.
27 A. Taflove and S. C. Hagness, *Computational Electrodynamics: The Finite-Difference Time-Domain Method*, Artech House, Incorporated, 2005.
28 J. D. Jackson, *Classical electrodynamics*, Wiley, New York, NY, 3rd edn, 1999.
29 F. Schedin, E. Lidorikis, A. Lombardo, V. G. Kravets, A. K. Geim, A. N. Grigorenko, K. S. Novoselov and A. C. Ferrari, *ACS Nano*, 2010, **4**, 5617.
30 E. D. Palik, *Handbook of Optical Constants of Solids*, Academic Press, 1998.
31 F. P. Incropera, *Fundamentals of Heat and Mass Transfer*, John Wiley & Sons, 2006.
32 D. R. Lide, *CRC Handbook of Chemistry and Physics*, Taylor & Francis, 85th edn, 2004.
33 S. Nolte, C. Momma, H. Jacobs, A. Tünnermann, B. N. Chichkov, B. Wellegehausen and H. Welling, *J. Opt. Soc. Am. B*, 1997, **14**, 2716.
34 A. Siozios, N. Kalfagiannis, D. V. Bellas, C. Bazioti, G. P. Dimitrakopulos, G. Vourlias, W. M. Cranton, E. Lidorikis, D. C. Koutsogeorgis and P. Patsalas, *Nanotechnology*, 2015, **26**, 155301.
35 F. Stietz, *Appl. Phys. A: Mater. Sci. Process.*, 2001, **72**, 381.
36 V. Mazumder, M. F. Chi, K. L. More and S. H. Sun, *Chem. Int. Ed.*, 2010, **49**, 9368.

 This journal is © The Royal Society of Chemistry 2016

Electronic Supplementary Material (ESI) for Nanoscale.
This journal is © The Royal Society of Chemistry 2016

Supplementary Information

Selective MOdification of Nanoparticle Arrays by Laser-Induced Self Assembly (*MONA-LISA*): putting control into bottom-up plasmonic nanostructuring

Nikolaos Kalfagiannis[1], Anastasios Siozios[2], Dimitris V. Bellas[2], Dimosthenis Toliopoulos[2], Leon Bowen[3], Nikolaos Pliatsikas[4], Wayne M. Cranton[1,5], Constantinos Kosmidis[6], Demosthenes C. Koutsogeorgis[1], Elefterios Lidorikis[2], Panos Patsalas[4]*

Summary: This supplementary information contains extensive experimental results that corroborate the results and conclusions presented in the manuscript, but due to their extent cannot fit in the manuscript. The manuscript refers to specific sections here, but in its entirety this document presents the complete results of our *MONA-LISA* work.

CONTENTS:

1. *LISA* and *MONA-LISA* by UV lasers (ArF: 193 nm and KrF: 248 nm)
   1.1. Contour plots vs. fluence and number of pulses for each wavelength
   1.2. Optical Reflectivity Spectra (ORS) of Ag thin films
      i. Ag thin films deposited by magnetron sputtering
      ii. Ag thin films deposited by alternative techniques
   1.3. ORS of Au thin films
   1.4. ORS of Cu thin films
2. VIS *MONA-LISA* of thin films
   2.1. Combined irradiations of UV (248 nm) and VIS (532 nm) on Ag thin films
      i. Ag thin films deposited by magnetron sputtering
      ii. Ag thin films deposited by e-beam evaporation
   2.2. Combined irradiations of UV (248 nm) and VIS (532 nm) on Au thin films
   2.3. Combined irradiations of UV (248 nm) and VIS (620 nm) on Ag thin films
3. Reproducibility tests
4. Microscopy Evaluation
5. Details of the Laser Annealing experimental set up

1. *LISA* and *MONA-LISA* by UV lasers (ArF: 193 nm and KrF: 248 nm)

The Table below summarizes the materials (metals) used in the present work, the deposition techniques used and the laser annealing processes that followed. These samples where then characterized by Optical Reflectivity Spectroscopy (ORS), Atomic Force microscopy (AFM) and Scanning Electron Microscopy (SEM). The experimental setup of the aforementioned techniques is adequately described in the experimental session of the manuscript.

Table i. Seed materials developed for the present work.

Metallic Layer[)]	Film Structure	Deposition Technique	Laser Annealing
Ag	Ag (5nm) / SiO_2 (2 nm) / Si Ag (10nm) / SiO_2 (2 nm) / Si	MS, EBE, Chemical	UV LA: 1. 193 nm (ArF) 2. 248 nm (KrF) VIS LA: 1. 532 nm (SHG, Nd:YAG) 2. 620 nm (OPO, Nd:YAG)
Au	Au (5nm) / SiO_2 (2 nm) / Si Au (10nm) / SiO_2 (2 nm) / Si	MS	UV LA: 1. 193 nm (ArF) 2. 248 nm (KrF) VIS LA: 1. 532 nm (SHG, Nd:YAG)
Cu	Cu (5nm) / SiO_2 (2 nm) / Si Cu (10nm) / SiO_2 (2 nm) / Si	MS	UV LA: 1. 193 nm (ArF) 2. 248 nm (KrF)

MS: magnetron sputtering, EBE: e-beam evaporation, Chemical: Referring to chemical reduction of AgNO3, UV: ultraviolet, VIS: Visible, SHG: second harmonic generator, OPO: optical parametric oscillator

Fig. S1 shows digital photos of Ag samples (10 nm of effective thickness), on 4” Si wafers, after laser processing with 193 nm (Fig. S1a) and 248 nm (Fig. S1b), respectively. The spots reveal palettes of various colours, depicting the variation of plasmonic responses at each set of LA conditions, spanning from red to blue.

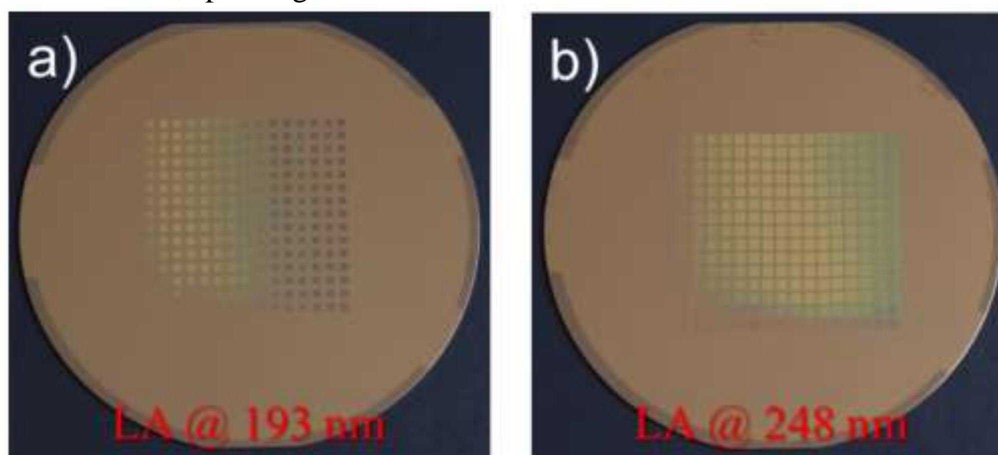

Figure S1. Digital photos of a Ag thin film (effective thickness of 10 nm) laser processed with (a) an ArF laser source emitting light at 193 nm and (b) a KrF source emitting light at 248 nm.

The laser spot delivered onto the samples was set, by an appropriate mask, to be a 2.0×2.0 mm^2 spot, for the case of 193 nm and 2.5×2.5 mm^2 spot, for the case of 248 nm. The variation in the spot sizes arises from the fact that the two laser sources have slightly different raw beam spot sizes and different beam delivery systems are used (see below for details of the LA experimental set up, section 5). The fluence varied from 200 mJ/cm^2 to 1000 mJ/cm^2 (left-to-right columns), using a step of 50 mJ/cm^2 and applying 1 to 15 (bottom-to-top) pulses (repetition rate was set at 1Hz). Single pulse UV LA is referred to as *LISA* process whereas successive UV laser pulses are referred to as UV *MONA-LISA*.

1.1. Contour plots vs fluence and number of pulses for each wavelength.

- **Ag (10nm) – LA@193 nm**: Fig. S2a and S2b present a map of the localised surface plasmon resonance (LSPR) spectral position and the reflectivity percentage at the LSPR, respectively. The results derived from the ORS spectra of each one of the LA spots. This map can provide a recipe that allows the design of plasmonic templates by UV LA. A green – yellowish response (530 – 570 nm) is observed by the spots that were produced under applied fluence between 200 and 500 mJ/cm^2. Above 450 mJ/cm^2 a gradual decrease in % reflectivity (%R) values is observed after the 4th pulse (where the maximum %R is reached), an indication of some loss of material due to ablation, concomitantly with a blueshift of the LSPR peak (due to larger empty space between particles). Above 650 mJ/cm^2 the laser process is ablating most of the material and as a consequence no LSPR peaks are apparent in the spectra; thus in Fig. S2 we present the contour plots only up to 650 mJ/cm^2. Note that at 250 mJ/cm^2 we can achieve the greatest variation of LSPR wavelengths and %R, where the saturation appears in high number of pulses contrary to all the other fluences applied.

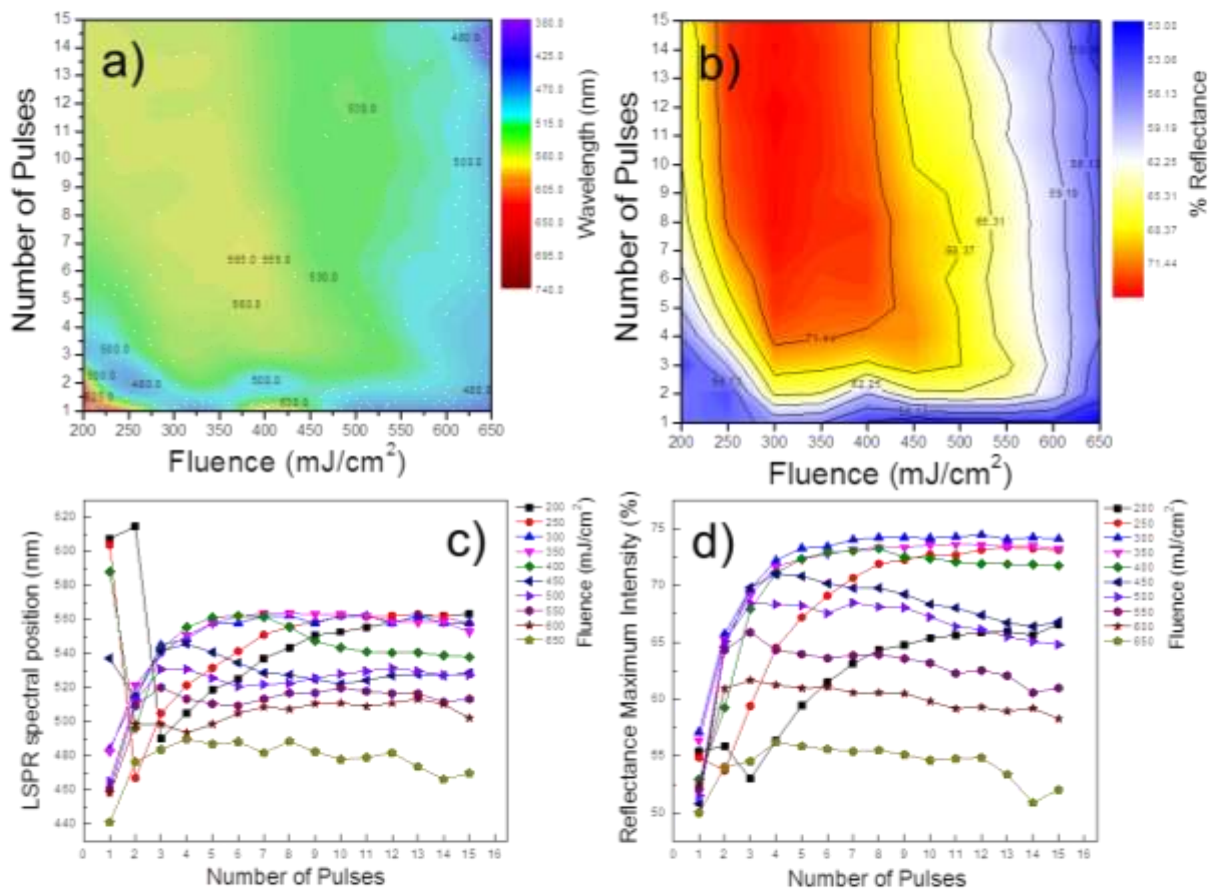

Figure S2. *LISA* / UV *MONA-LISA* (193 nm) of a Ag thin film with an effective thickness of 10 nm: (a) a contour plot of the dominant LSPR spectral position for the various number of pulses and applied fluence during LA, (b) a contour plot of the maximum reflectivity of the dominant LSPR for the various number of pulses and fluence applied during LA, (c) dominant LSPR spectral position for the various number of pulses under different applied fluence and (d) maximum reflectivity of the dominant LSPR for the various number of pulses under different applied fluence.

- **Ag (10nm) – LA@248 nm**: The overall behaviour of the sample under 248 nm exposure is the same as under the 193 nm. However, in this case, the optical response of the vast majority of the selected LA conditions is positioned in the green – yellowish range, between 530 and 575 nm. At the same time, for the same conditions, the maximum reflectivity percentage (%R) is achieved, varying from 70 – 75 %. However, it is remarkable that we manage to get a broad variation in plasmonic response, from 465 nm to as high as the limit of the VIS spectral range (735 nm for low fluence and low number of pulses).

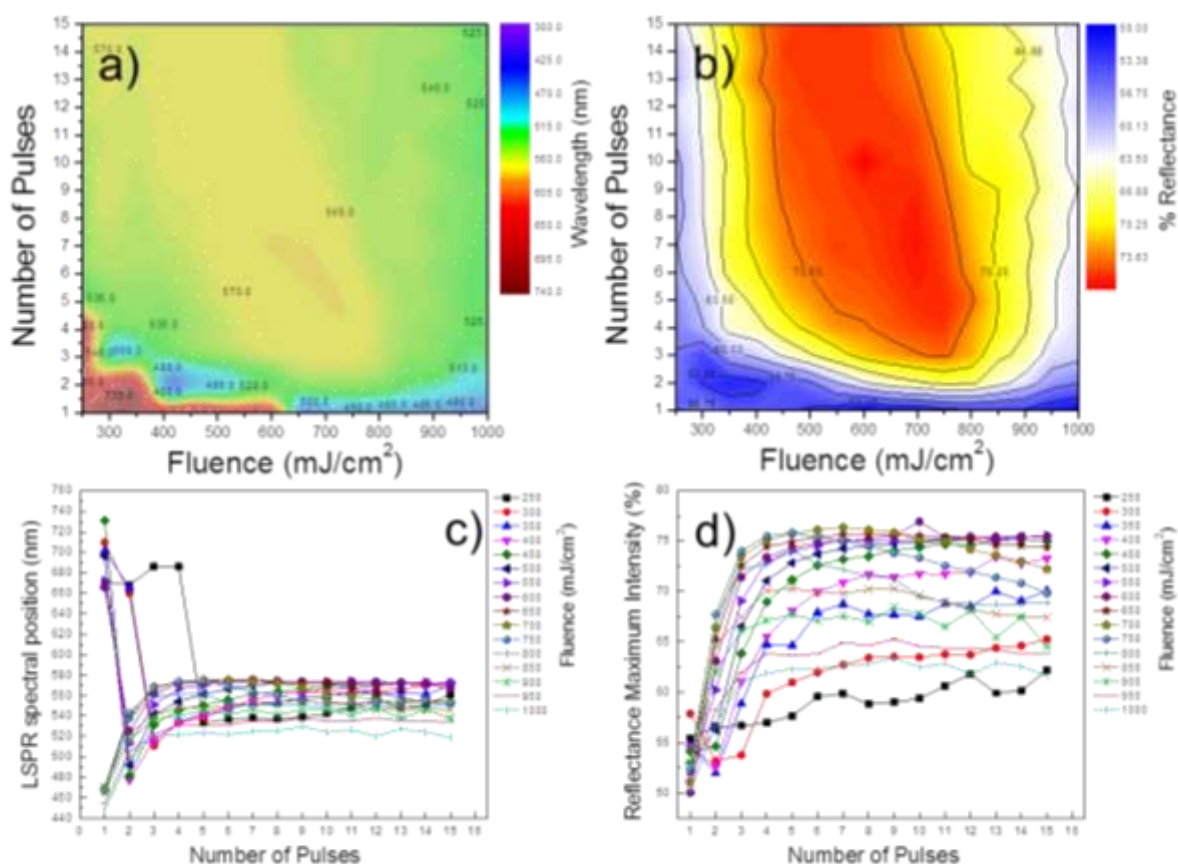

Figure S3. *LISA* / UV *MONA-LISA* (248 nm) of a Ag thin film with an effective thickness of 10 nm: (a) a contour plot of the dominant LSPR spectral position for the various number of pulses and applied fluence during LA, (b) a contour plot of the maximum reflectivity of the dominant LSPR for the various number of pulses and fluence applied during LA, (c) dominant LSPR spectral position for the various number of pulses under different applied fluence and (d) maximum reflectivity of the dominant LSPR for the various number of pulses under different applied fluence.

1.2 Optical Reflectivity Spectra (ORS) of Ag thin films

The number of samples that have been processed in the framework of this work is in the order of several thousands. That makes it practically impossible to present all those spectra (from which the previous colour maps derived). Alternatively, we chose to present results of some selective, representative conditions. These representative conditions were chosen for the experimental part of VIS *MONA-LISA*, comprising the UV LA (*LISA* / UV *MONA-LISA*) template to which the VIS LA (either 532 nm or 620 nm) applied.

The following figure (Fig. S4) presents ORS spectra of selective conditions of Ag samples (5 and 10 nm of effective thickness) processed by 193 nm and 248 nm LA.

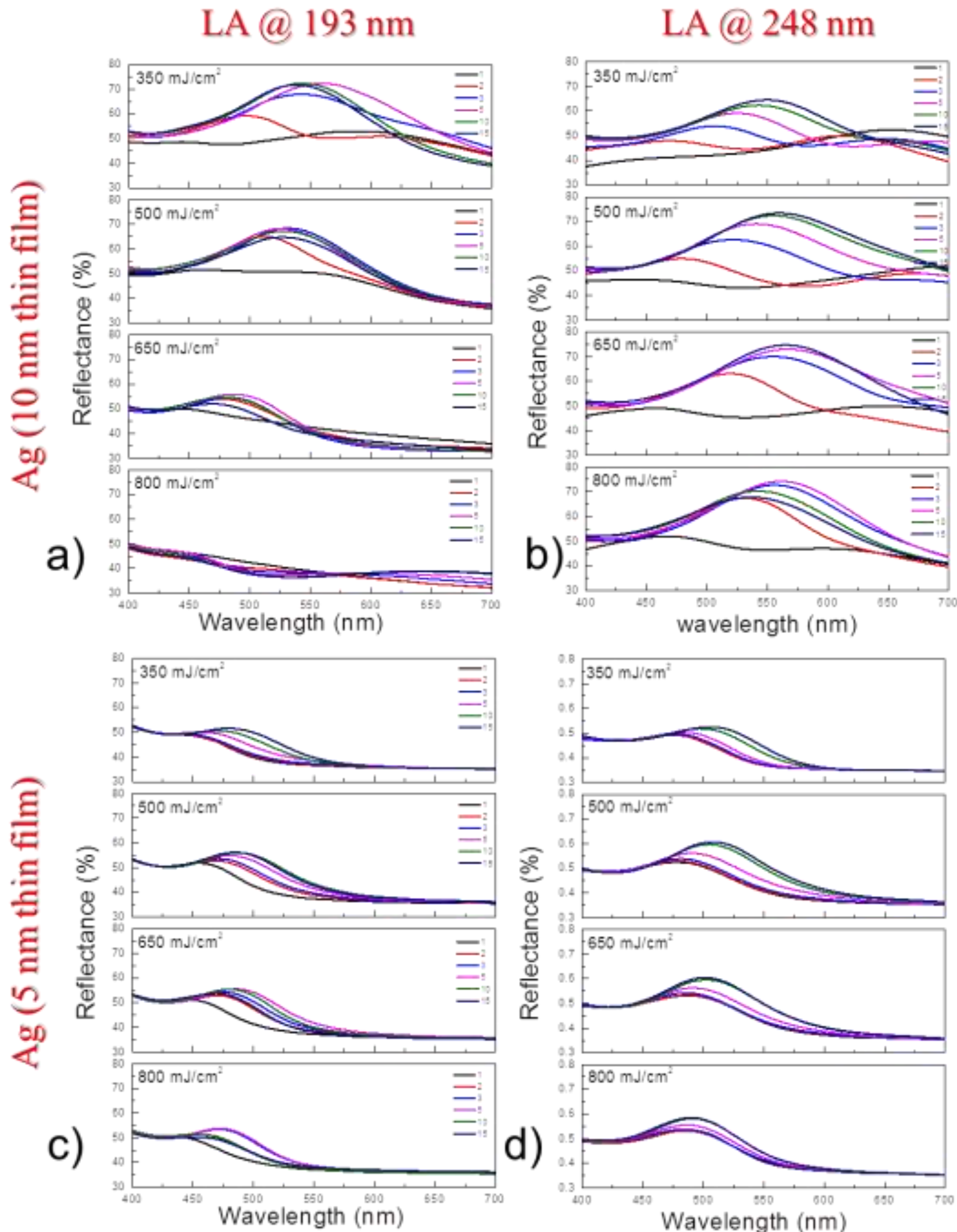

Figure S4. Optical reflectivity spectra of (a) *LISA* / UV *MONA-LISA* (193 nm) of a 10 nm Ag thin film, (b) *LISA* / UV *MONA-LISA* (248 nm) of a 10 nm Ag thin film, (c) *LISA* / UV *MONA-LISA* (193 nm) of a 5 nm Ag thin film and (d) *LISA* / UV *MONA-LISA* (248 nm) of a 5 nm Ag thin film.

1.3. ORS of Au thin Films

The following figure (Fig. S5) presents ORS spectra of selective conditions of Au samples (5 and 10 nm of effective thickness) processed by 248 nm LA.

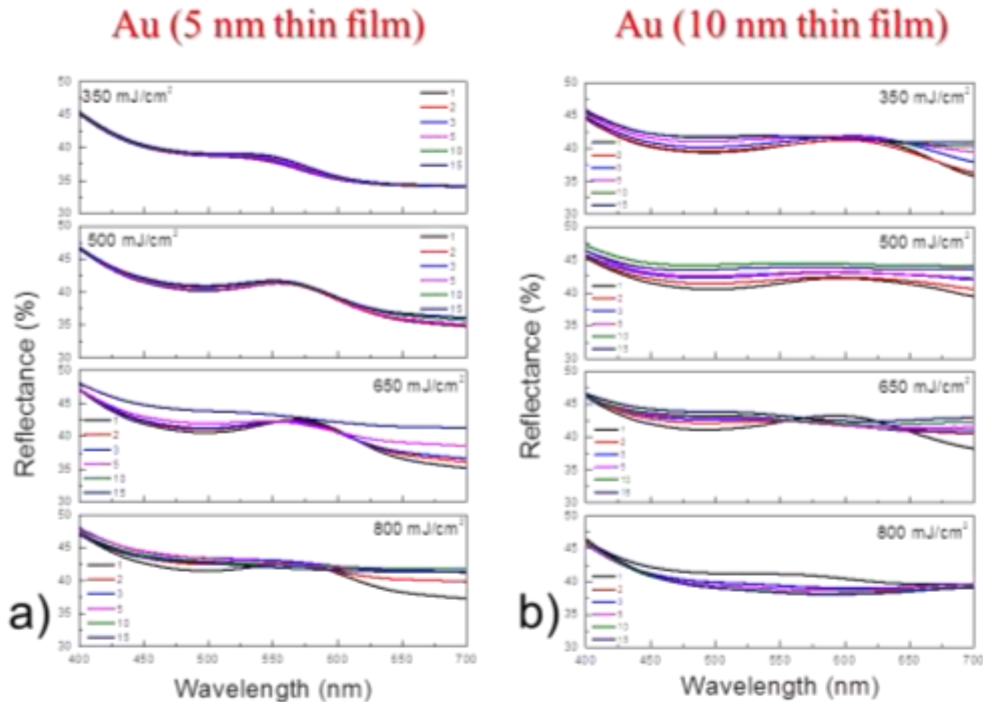

Figure S5. Optical reflectivity spectra of (a) *LISA* / UV *MONA-LISA* (248 nm) of 5 nm Au thin film and (b) *LISA* / UV *MONA-LISA* (248 nm) of 10 nm Au thin film.

1.4. ORS of Cu thin Films

The following figure (Fig. S6) presents ORS spectra of selective conditions of Cu samples (5 and 10 nm of effective thickness) processed by 248 nm LA.

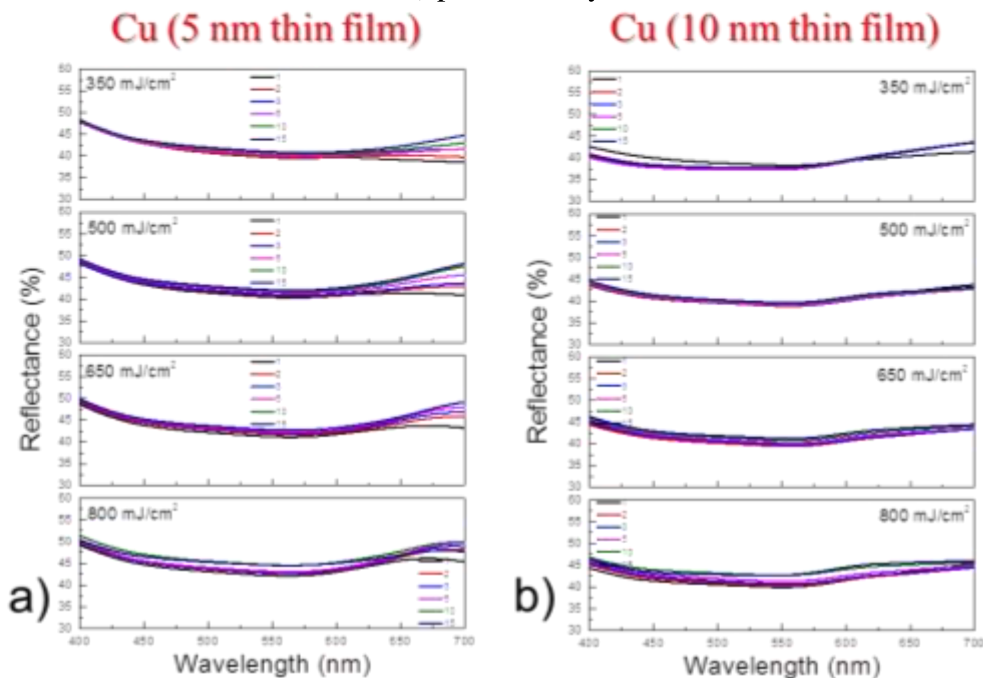

Figure S6. Optical reflectivity spectra of (a) *LISA* / UV *MONA-LISA* (248 nm) of 5 nm Cu thin film and (b) *LISA* / UV *MONA-LISA* (248 nm) of 10 nm Cu thin film.

2. VIS *MONA-LISA* of thin films

In this part of the supplementary information we describe the combined processes of UV LA (at 248 nm) and subsequent exposure to a Nd:YAG laser set with the second harmonic generator (SHG) to emit light at 532 nm or set with an optical parametric oscillator (OPO) unit to emit light at 620 nm (OPO is pumped with the third harmonic of Nd:YAG – 355 nm). We present the optical reflectivity spectra along side the scanning electron microscopy imaging, and in direct comparison between the initial UV LA and the UV LA followed by the VIS LA processes (the process which we call VIS *MONA-LISA*). The beam delivery path for the Nd:YAG laser comprised three mirrors, a variable attenuator to control the energy density of each pulse (6 ns in duration) and a round aperture allowing a 2 mm diameter round spot to reach the samples' surface. The repetition rate was set at 10 Hz.

2.1 Combined irradiations of UV (248 nm) and VIS (532 nm) on Ag thin films

i. Ag thin films deposited by magnetron sputtering

As mentioned above, under UV exposure the plasmonic response of the samples saturated after the first 4-5 pulses. Further tailoring of the plasmonic response can be achieved by delivering extra nanosecond pulses at a wavelength matching their LSPR.

To establish an initial processing window for the VIS LA treatment on the UV LA samples, we investigated the effect of fluence and number of pulses over a specific UV LA condition; 10 pulses (248 nm) at 650 mJ/cm^2, which gives a good plasmonic response close to 532 nm. As a starting point we began with very low fluence (25 mJ/cm^2). Up to 75 mJ/cm^2 and for thousands of pulses the sample's optical response was not altered. Above 75 mJ/cm^2 the sample changed its optical properties; a slight blueshift occurred concomitantly with a reduction of the spectral width. At 100 mJ/cm^2 similar observations were made. We found that the optimum condition was the application of 500 pulses at 125 mJ/cm^2 (Fig. S7c). We treated the whole UV LA sample grid of Fig. S8 (right) with the VIS (532 nm) LA applying 500 pulses at 125 mJ/cm^2 with a repetition rate of 10 Hz.

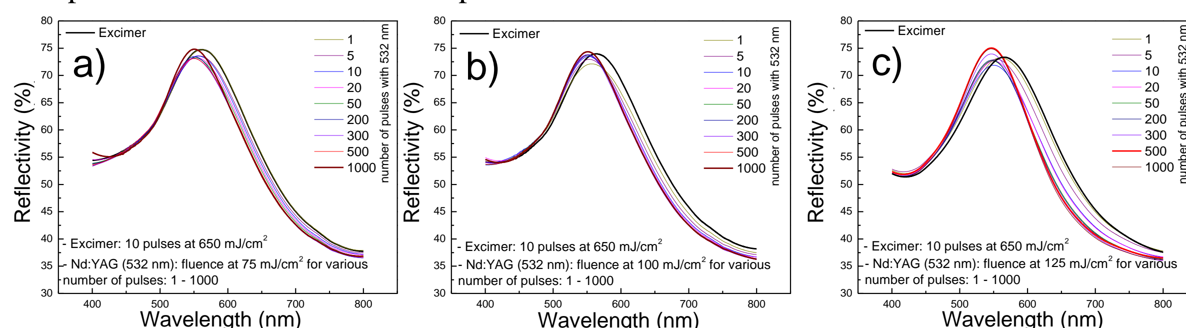

Figure S7. VIS LA (532 nm) of a sample previously processed with UV (248 nm) LA with 10 pulses at 650 mJ/cm^2. The choice of this particular condition of UV LA was made due to the optical response of the sample, showing a high plasmonic response close to 532 nm. Three fluences were tested for various number of pulses in order to find the optimum condition for the VIS LA: (a) 75 mJ/cm^2, (b) 100 mJ/cm^2 and (c) 125 mJ/cm^2.

Figure S8 shows digital photos of the sample grids used for the *LISA* / UV *MONA-LISA*, shown on the right, and of the same UV LA produced grid that subsequently was processed with the VIS *MONA-LISA*, shown on the left. Note that the VIS spot is round (2 mm in diameter) and is well placed at the centre of the square UV LA spot (2.5x2.5mm^2). Also note the colour variations in the spots of the *LISA* / UV *MONA-LISA* process in comparison to the VIS *MONA-LISA* process, especially those with visual appearance far away from the green. Processing with the VIS LA shifts the colour to the green, an observation that is accompanied by shift of the plasmon peak towards wavelengths close to 532 nm.

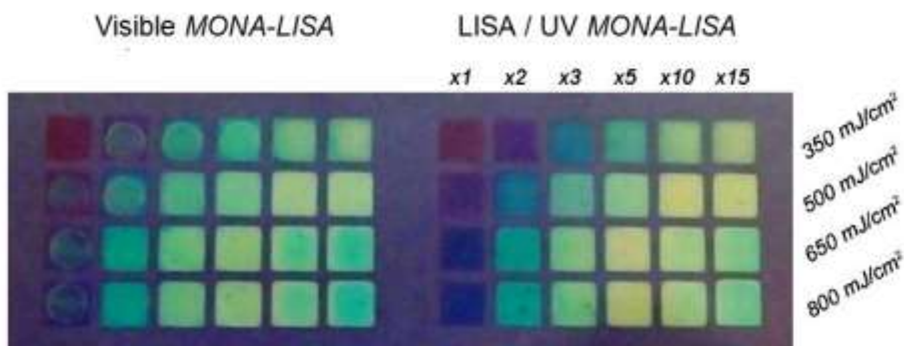

Figure S8. Digital photos of the sample grids used for irradiation with the UV laser (248 nm), shown on the right (*LISA* / UV *MONA-LISA*), and a combined irradiation with UV and VIS (532nm), shown on the left (VIS *MONA-LISA*). Note that the VIS spot is circular (2 mm in diameter). Also note the colour variation in the spots with visual appearance far away from the green.

The following figure (Fig. S9) presents a collage of SEM images in direct reference to the above-mentioned sample grids. The SEM snapshots of the spots corresponding to the VIS *MONA-LISA* processes are on the left, while on the right side are snapshots of the *LISA* / UV *MONA-LISA* template. Size distributions and shape variations can be observed.

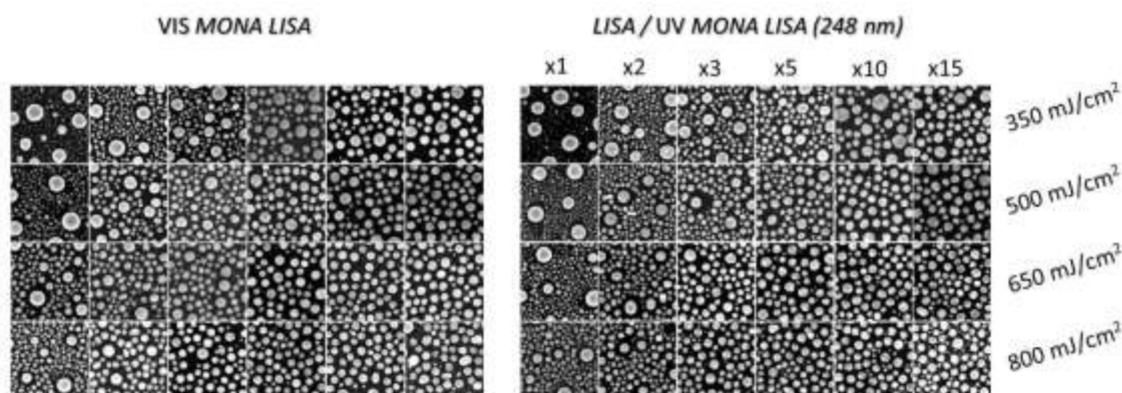

Figure S9. SEM snapshots of the corresponding sample grids shown in Fig. S8: *LISA* / UV *MONA-LISA* (248 nm) is shown on the right, and VIS *MONA-LISA* is shown on the left.

In the following paragraphs we present analytically the ORS graphs, SEM imaging and the statistical analysis of the *MONA-LISA* process. Since the *LISA* / UV *MONA-LISA* grid was used as a template for the VIS *MONA-LISA* process we entitle each case with the fluence used during the UV exposure. For the reader's convenience the black coloured lines, bars and SEM figure boarders refer to the *LISA* / UV *MONA-LISA* process whereas the red coloured lines, bars and SEM figure boarders refer to the VIS *MONA-LISA* (combined UV & VIS LA) process. Finally, in all the ORS graphs the green dashed line sets the wavelength used for the VIS LA experiment (532 nm).

LISA / UV *MONA-LISA* (248 nm, 350 mJ/cm^2)

1 pulse of UV & 1 pulse of UV plus VIS treatment

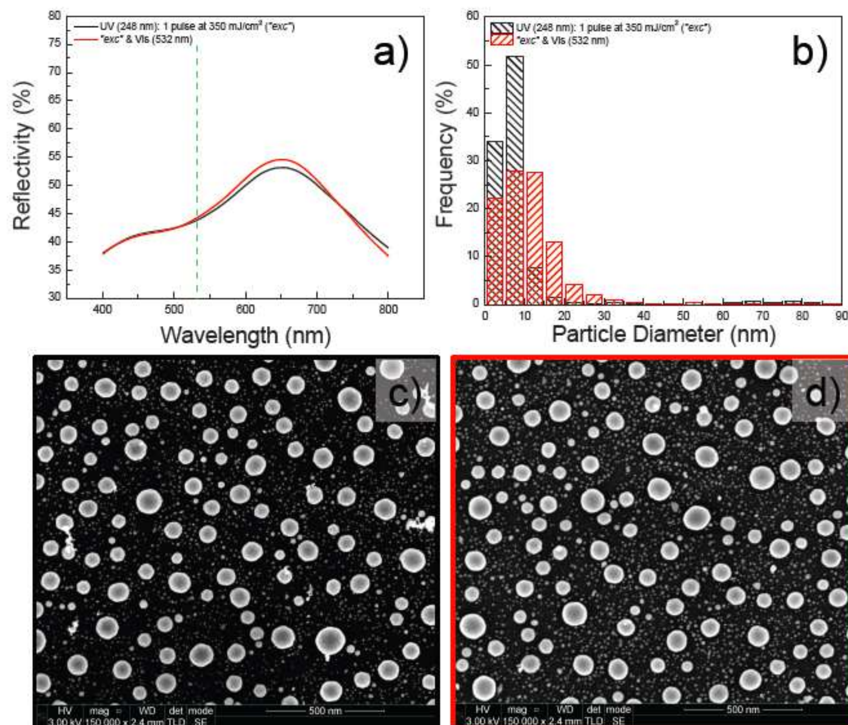

Figure S10. (a) ORS of the UV LA, 1 pulse at 350 mJ/cm^2 (black line), used as a template for the subsequent VIS LA process, 500 pulses at 125 mJ/cm^2 (red line), (b) Particle size distributions derived from SEM imaging analysis of the sample processed with the UV LA (black shaded bars) and the sample treated with the UV LA and the VIS LA (red shaded bars), (c) SEM image of the UV LA processed sample and (d) SEM image of the UV LA and VIS LA processed sample.

2 pulses of UV & 2 pulses of UV plus VIS treatment

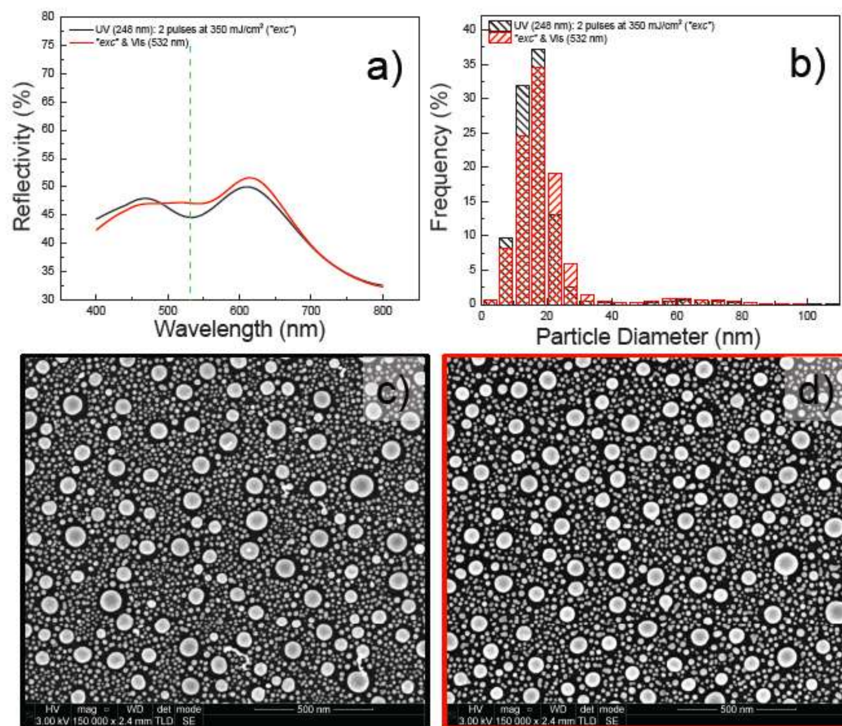

Figure S11. (a) ORS of the UV LA, 2 pulses at 350 mJ/cm^2 (black line), used as a template for the subsequent VIS LA process, 500 pulses at 125 mJ/cm^2 (red line). The green dashed line sets the 532 nm mark. (b) Particle size distributions derived from SEM imaging analysis of the sample processed with the UV LA (black shaded bars) and the sample treated with the UV LA and the VIS LA (red shaded bars), (c) SEM image of the UV LA processed sample and (d) SEM image of the UV LA and VIS LA processed sample.

For this particular sample we further investigated an increased number of pulses and we present results for VIS LA at 2000 and 4000 pulses. The results are shown in Fig. S12: The underlying template produced via UV LA shows a bimodal response with two clear bands, one close to 450 nm and another one close to 600 nm (black line). At 500 pulses of VIS LA a new plasmonic band, makes its appearance close to the 532 nm (red line). This band evolves as we further treat the sample with 2000 pulses (blue line) and can be now more clearly seen. In this case a clear triple plasmonic peak is observed. As we continue to treat the sample with more pulses (4000) the two peaks at higher wavelengths begin to overlap. This process could be seen as a “plasmonic evolution” process, which resembles the evolution by natural selection: only the particles with LSPR at 532 nm will eventually “survive”.

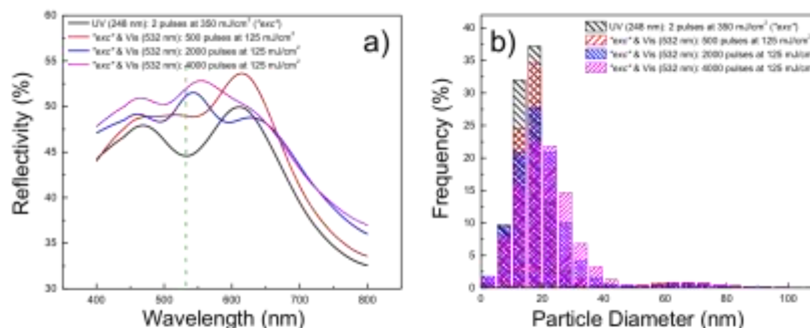

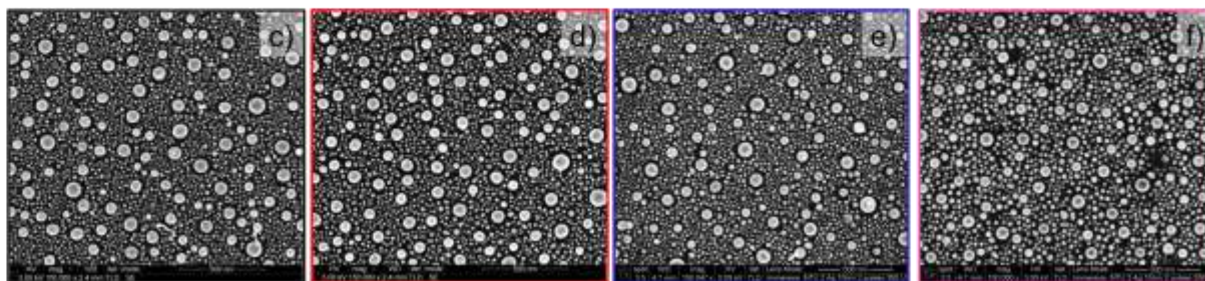

Figure S12. (a) ORS of the UV LA, 2 pulse at 350 mJ/cm^2 (black line), used as a template for the subsequent VIS LA process, 500 pulses (red line), 2000 pulses (blue line) and 4000 pulses (magenta line) at 125 mJ/cm^2. The green dashed line sets the 532 nm mark. (b) Particle size distributions derived from SEM imaging analysis of the sample processed with the UV LA (black bars) and the sample treated with the UV LA and the VIS LA at 500 pulses (red bars), 2000 pulses (blue bars) and 4000 pulses (magenta bars), (c) SEM image of the UV LA processed sample, (d) SEM image of the UV LA and VIS LA processed sample at 500 pulses, (e) SEM image of the UV LA and VIS LA processed sample at 2000 pulses and (f) SEM image of the UV LA and VIS LA processed sample at 4000 pulses.

However, treatment at 4000 pulses produces “hot spots” in the film’s surface as shown in Fig. S13, where low magnification SEM images are presented. Up to 2000 pulses the sample’s surface is homogeneous and the VIS LA process is uniform throughout the surface. On the contrary, treatment at 4000 pulses produces irregularities on the surface morphology.

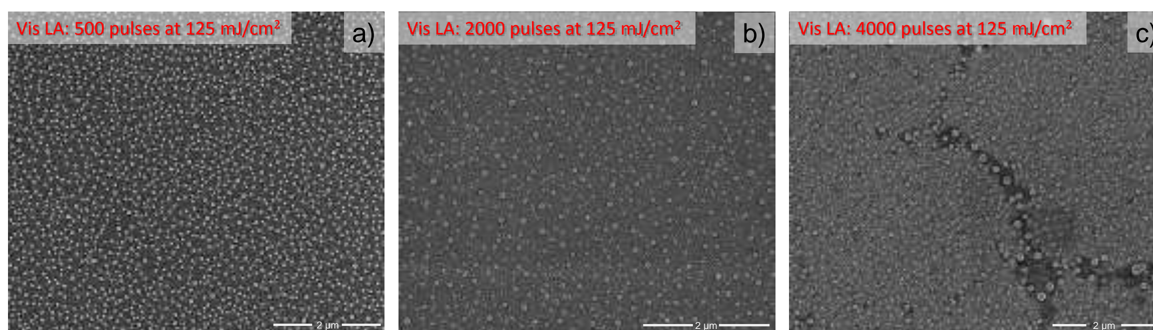

Figure S13. Lower magnification SEM images to show the uniformity of the samples produced with the VIS LA process. All samples were initially prepared with UV LA (2 pulses at 350 mJ/cm^2) and subsequently with VIS LA (532nm): (a) 500 pulses at 125 mJ/cm^2, (b) 2000 pulses at 125 mJ/cm^2 and (c) 4000 pulses at 125 mJ/cm^2 processed sample.

3 pulses of UV & 3 pulses of UV plus VIS treatment

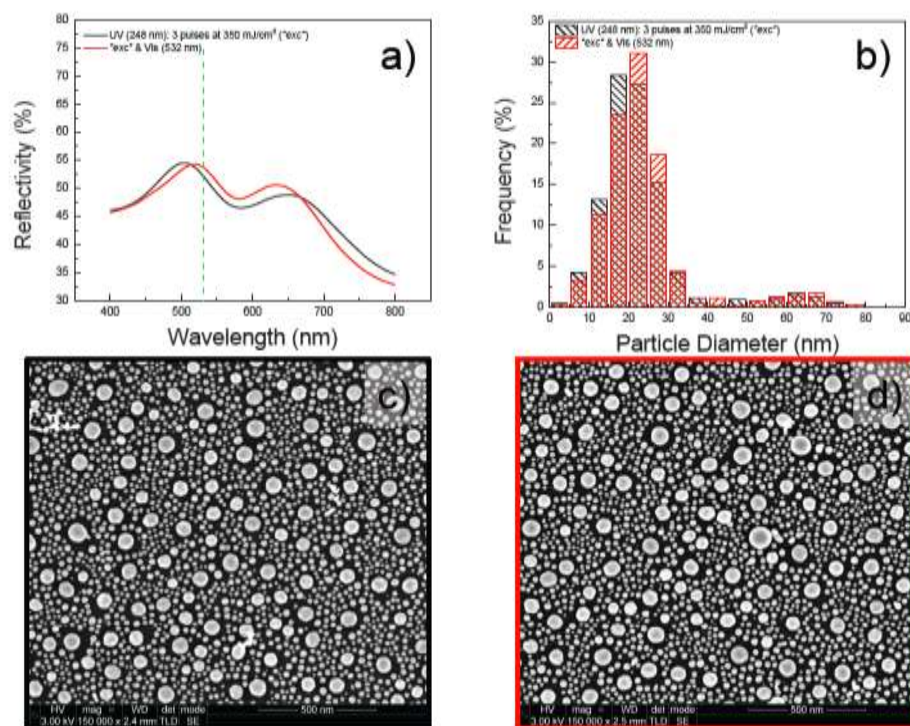

Figure S14. (a) ORS of the UV LA, 3 pulses at 350 mJ/cm^2 (black line), used as a template for the subsequent VIS LA process, 500 pulses at 125 mJ/cm^2 (red line). The green dashed line sets the 532 nm mark. (b) Particle size distributions derived from SEM imaging analysis of the sample processed with the UV LA (black shaded bars) and the sample treated with the UV LA and the VIS LA (red shaded bars), (c) SEM image of the UV LA processed sample and (d) SEM image of the UV LA and VIS LA processed sample.

5 pulses of UV & 5 pulses of UV plus VIS treatment

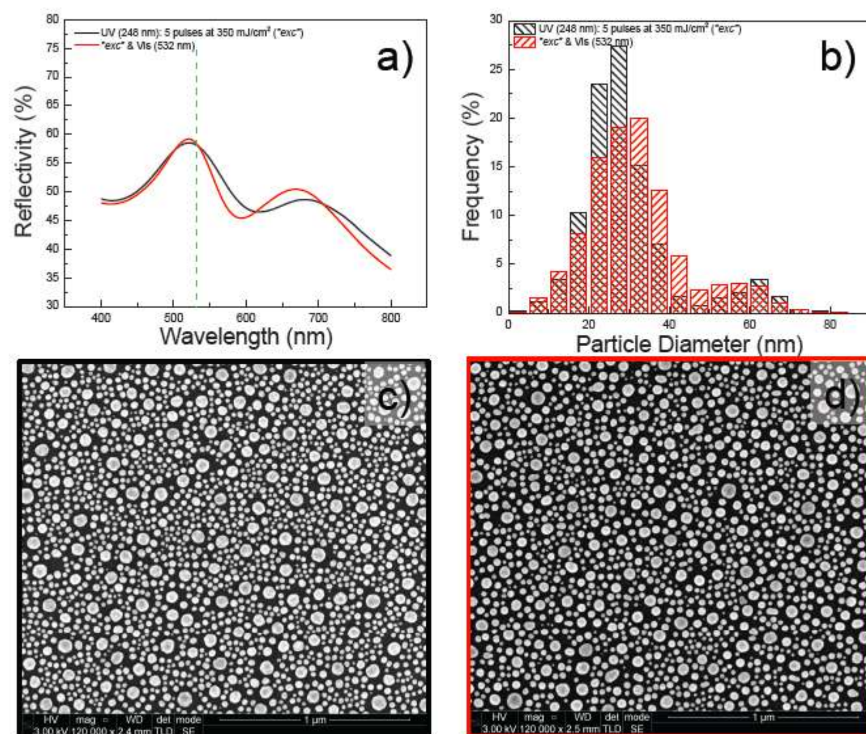

Figure S15. (a) ORS of the UV LA, 5 pulses at 350 mJ/cm^2 (black line), used as a template for the subsequent VIS LA process, 500 pulses at 125 mJ/cm^2 (red line). The green dashed line sets the 532 nm mark. (b) Particle size distributions derived from SEM imaging analysis of the sample processed with the UV LA (black shaded bars) and the sample treated with the UV LA and the VIS LA (red shaded bars), (c) SEM image of the UV LA processed sample and (d) SEM image of the UV LA and VIS LA processed sample.

10 pulses of UV & 10 pulses of UV plus VIS treatment

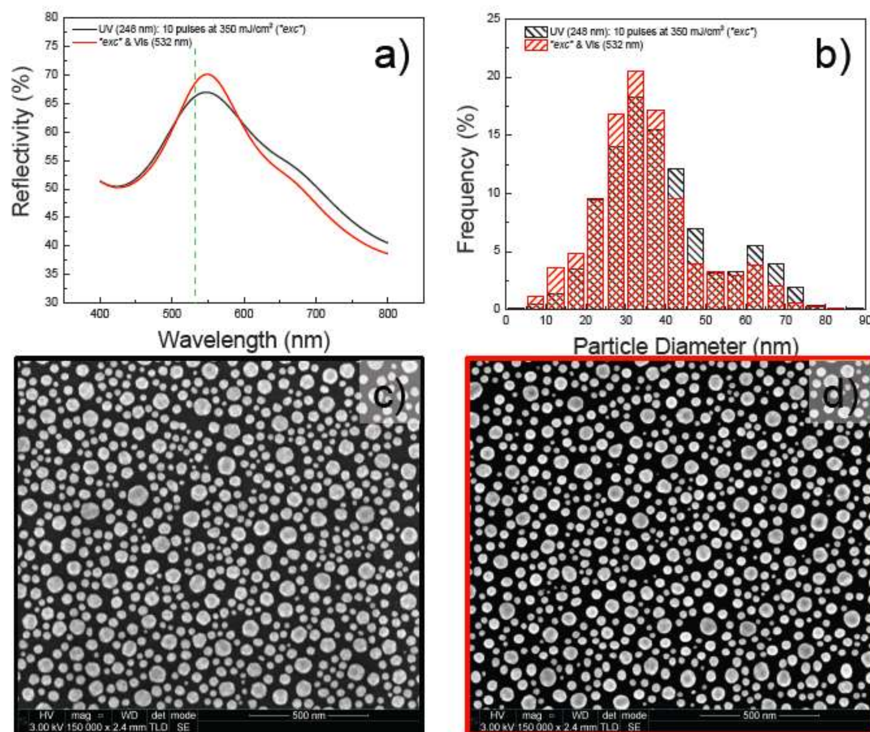

Figure S16. (a) ORS of the UV LA, 10 pulses at 350 mJ/cm^2 (black line), used as a template for the subsequent VIS LA process, 500 pulses at 125 mJ/cm^2 (red line). The green dashed line sets the 532 nm mark. (b) Particle size distributions derived from SEM imaging analysis of the sample processed with the UV LA (black shaded bars) and the sample treated with the UV LA and the VIS LA (red shaded bars), (c) SEM image of the UV LA processed sample and (d) SEM image of the UV LA and VIS LA processed sample.

15 pulses of UV & 15 pulses of UV plus VIS treatment

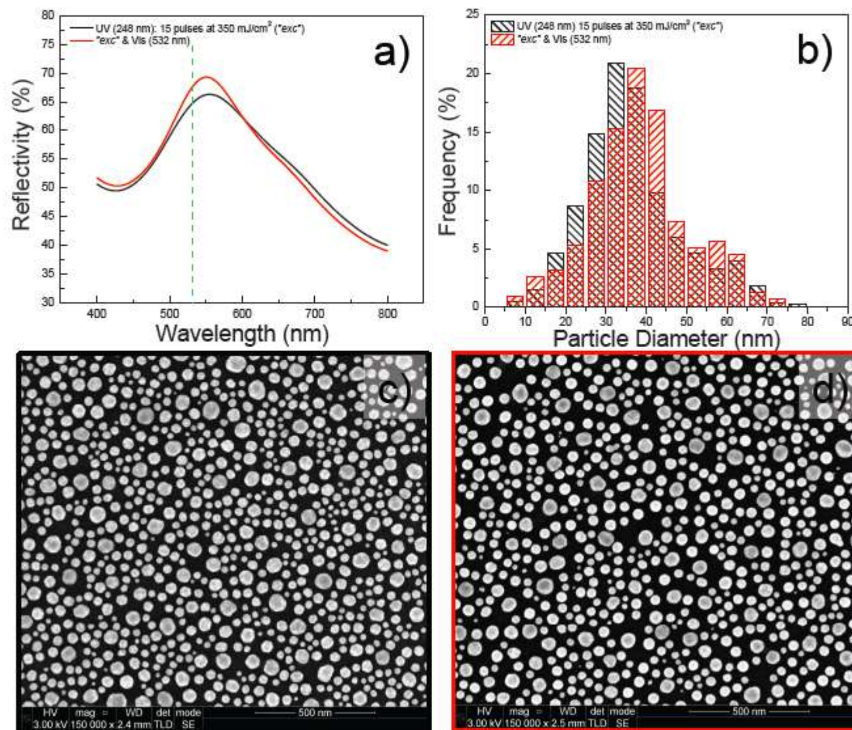

Figure S17. (a) ORS of the UV LA, 15 pulses at 350 mJ/cm^2 (black line), used as a template for the subsequent VIS LA process, 500 pulses at 125 mJ/cm^2 (red line). The green dashed line sets the 532 nm mark. (b) Particle size distributions derived from SEM imaging analysis of the sample processed with the UV LA (black shaded bars) and the sample treated with the UV LA and the VIS LA (red shaded bars), (c) SEM image of the UV LA processed sample and (d) SEM image of the UV LA and VIS LA processed sample.

LISA / UV *MONA-LISA* (248 nm, 500 mJ/cm^2)

1 pulse of UV & 1 pulse of UV plus VIS treatment

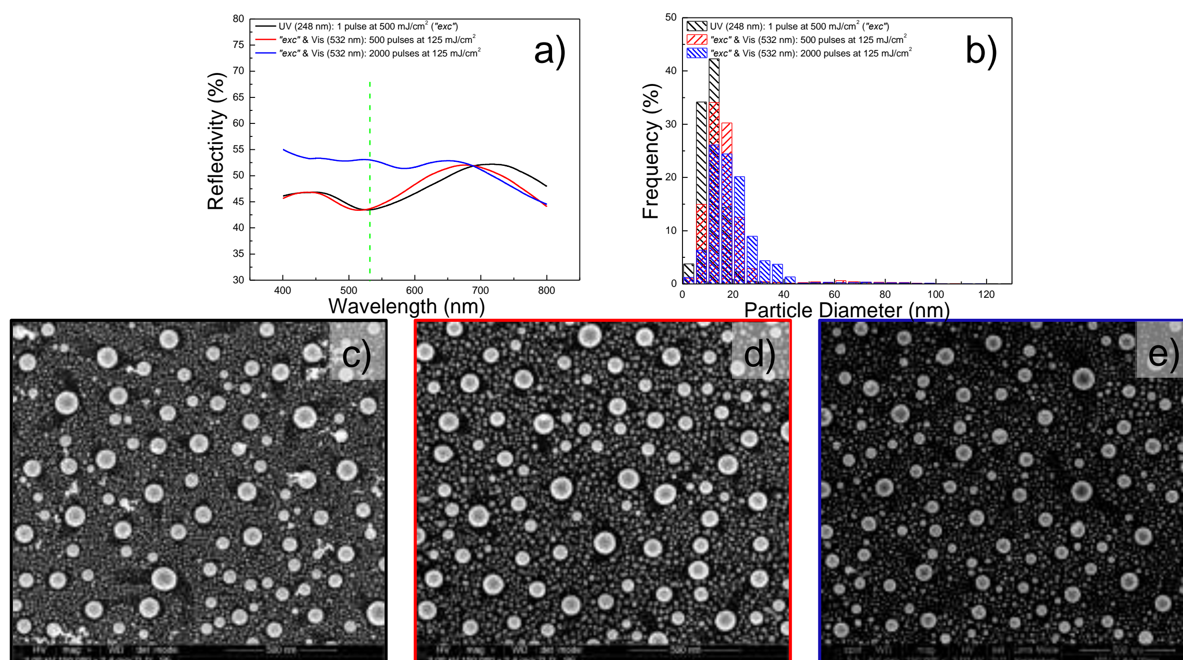

Figure S18. (a) ORS of the UV LA, 1 pulse at 500 mJ/cm^2 (black line), used as a template for the subsequent VIS LA process, 500 pulses (red line) and 2000 pulses (blue line) at 125 mJ/cm^2. The green dashed line sets the 532 nm mark. (b) Particle size distributions derived from SEM imaging analysis of the sample processed with the UV LA (black bars) and the sample treated with the UV LA and the VIS LA at 500 pulses (red bars) and 2000 pulses (blue bars) all at 125 mJ/cm^2, (c) SEM image of the UV LA processed sample, (d) SEM image of the UV LA and VIS LA processed sample at 500 pulses, (e) SEM image of the UV LA and VIS LA processed sample at 2000 pulses.

2 pulses of UV & 2 pulses of UV plus VIS treatment

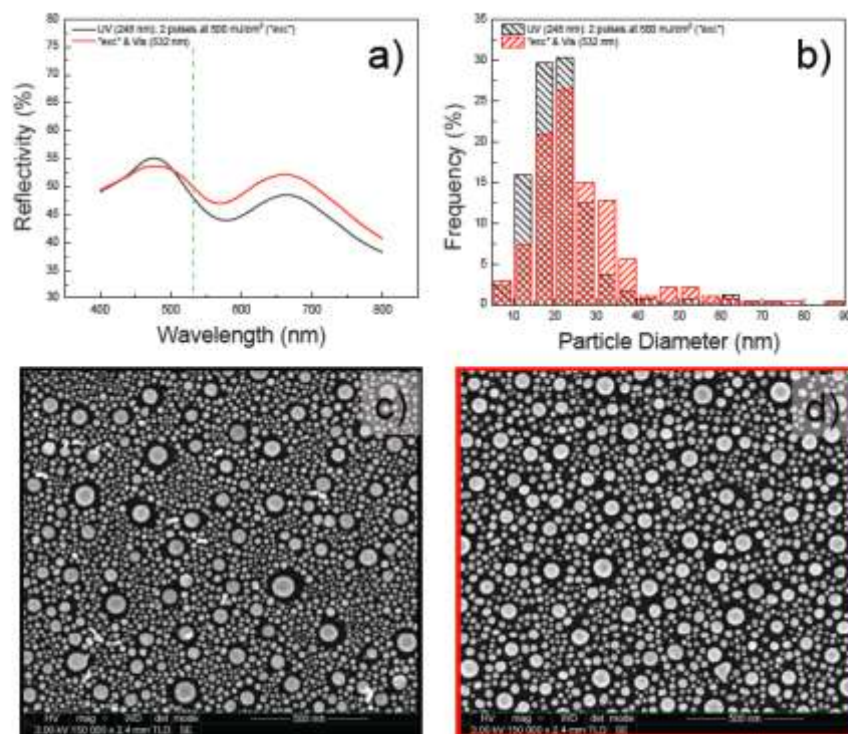

Figure S19. (a) ORS of the UV LA, 2 pulses at 500 mJ/cm^2 (black line), used as a template for the subsequent VIS LA process, 500 pulses at 125 mJ/cm^2 (red line). The green dashed line sets the 532 nm mark. (b) Particle size distributions derived from SEM imaging analysis of the sample processed with the UV LA (black shaded bars) and the sample treated with the UV LA and the VIS LA (red shaded bars), (c) SEM image of the UV LA processed sample and (d) SEM image of the UV LA and VIS LA processed sample.

3 pulses of UV & 3 pulses of UV plus VIS treatment

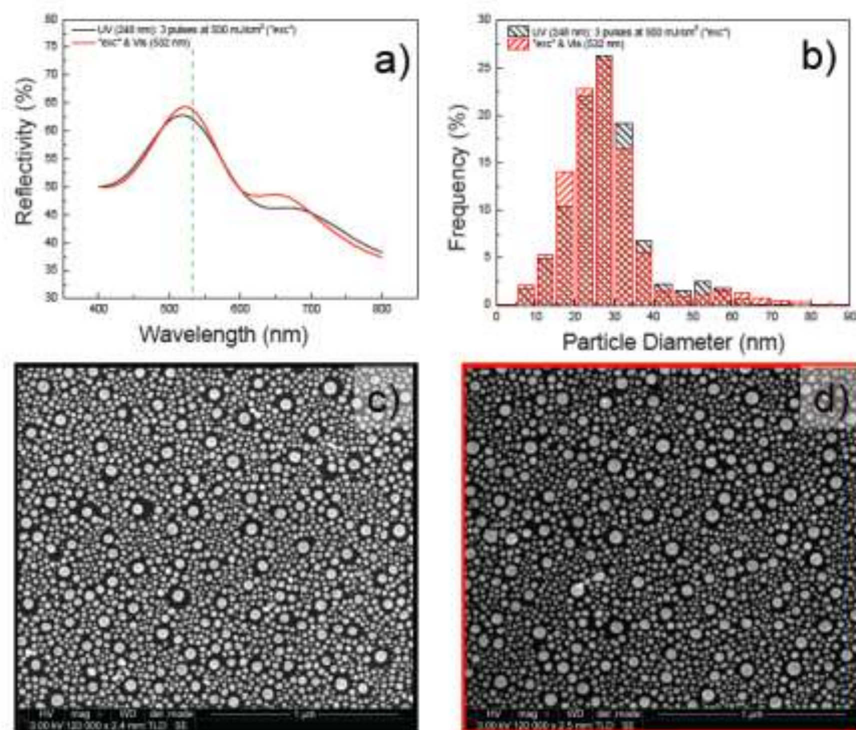

Figure S20. (a) ORS of the UV LA, 3 pulses at 500 mJ/cm^2 (black line), used as a template for the subsequent VIS LA process, 500 pulses at 125 mJ/cm^2 (red line). The green dashed line sets the 532 nm mark. (b) Particle size distributions derived from SEM imaging analysis of the sample processed with the UV LA (black shaded bars) and the sample treated with the UV LA and the VIS LA (red shaded bars), (c) SEM image of the UV LA processed sample and (d) SEM image of the UV LA and VIS LA processed sample.

5 pulses of UV & 5 pulses of UV plus VIS treatment

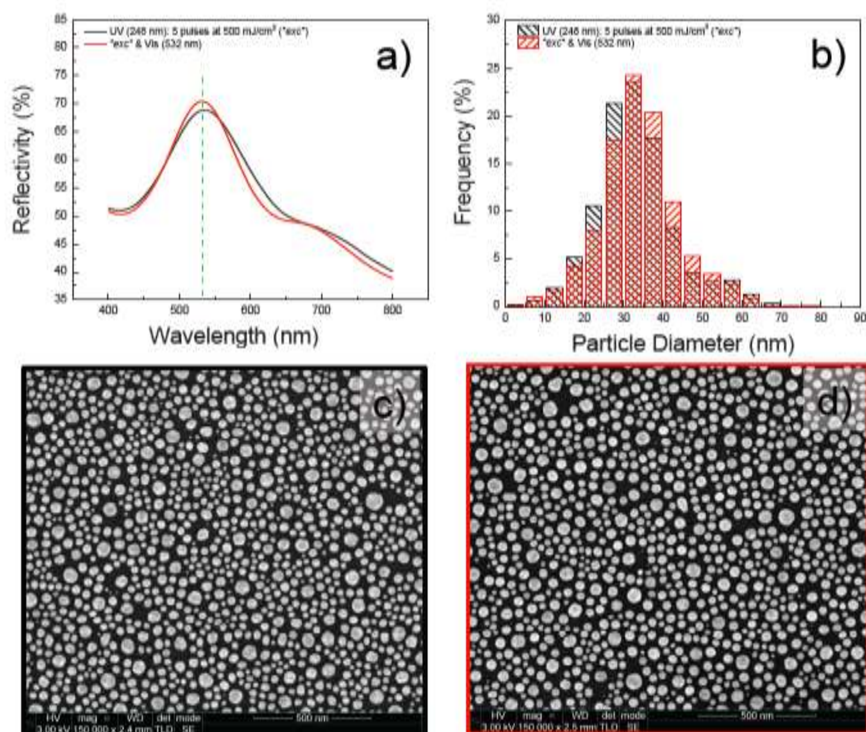

Figure S21. (a) ORS of the UV LA, 5 pulses at 500 mJ/cm^2 (black line), used as a template for the subsequent VIS LA process, 500 pulses at 125 mJ/cm^2 (red line). The green dashed line sets the 532 nm mark. (b) Particle size distributions derived from SEM imaging analysis of the sample processed with the UV LA (black shaded bars) and the sample treated with the UV LA and the VIS LA (red shaded bars), (c) SEM image of the UV LA processed sample and (d) SEM image of the UV LA and VIS LA processed sample.

10 pulses of UV & 10 pulses of UV plus VIS treatment

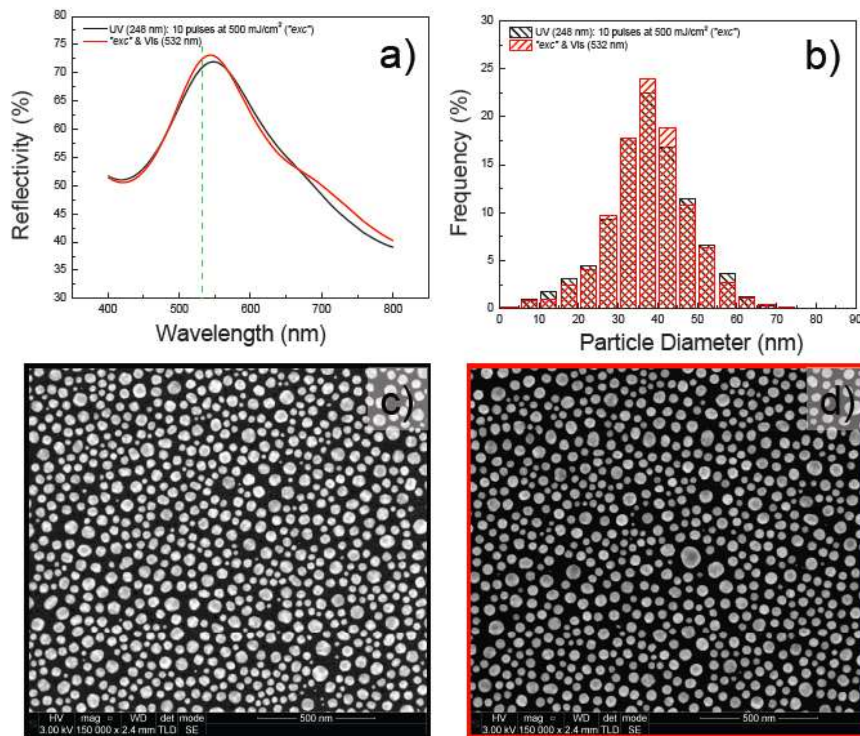

Figure S21. (a) ORS of the UV LA, 10 pulses at 500 mJ/cm^2 (black line), used as a template for the subsequent VIS LA process, 500 pulses at 125 mJ/cm^2 (red line). The green dashed line sets the 532 nm mark. (b) Particle size distributions derived from SEM imaging analysis of the sample processed with the UV LA (black shaded bars) and the sample treated with the UV LA and the VIS LA (red shaded bars), (c) SEM image of the UV LA processed sample and (d) SEM image of the UV LA and VIS LA processed sample.

15 pulses of UV & 15 pulses of UV plus VIS treatment

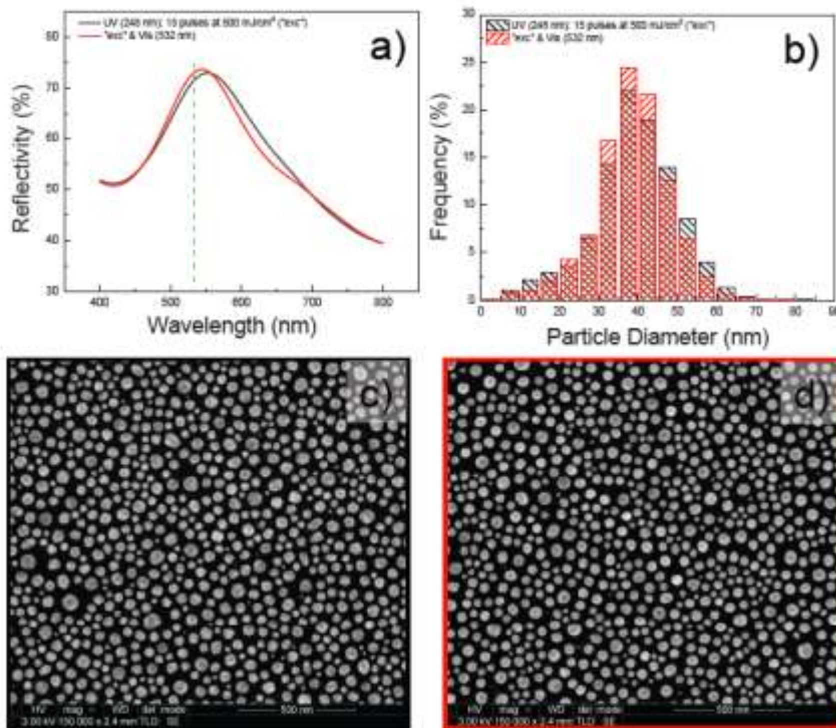

Figure S22. (a) ORS of the UV LA, 15 pulses at 500 mJ/cm^2 (black line), used as a template for the subsequent VIS LA process, 500 pulses at 125 mJ/cm^2 (red line). The green dashed line sets the 532 nm mark. (b) Particle size distributions derived from SEM imaging analysis of the sample processed with the UV LA (black shaded bars) and the sample treated with the UV LA and the VIS LA (red shaded bars), (c) SEM image of the UV LA processed sample and (d) SEM image of the UV LA and VIS LA processed sample.

LISA / UV *MONA-LISA* (248 nm, 650 mJ/cm^2)

1 pulse of UV & 1 pulse of UV plus VIS treatment

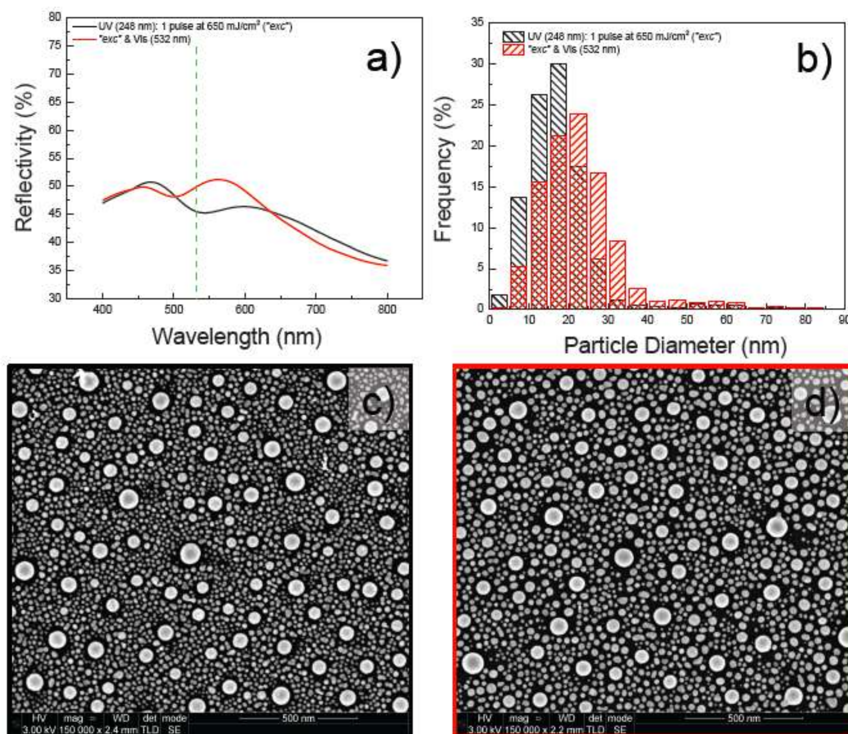

Figure S23. (a) ORS of the UV LA, 1 pulse at 650 mJ/cm^2 (black line), used as a template for the subsequent VIS LA process, 500 pulses at 125 mJ/cm^2 (red line). The green dashed line sets the 532 nm mark. (b) Particle size distributions derived from SEM imaging analysis of the sample processed with the UV LA (black shaded bars) and the sample treated with the UV LA and the VIS LA (red shaded bars), (c) SEM image of the UV LA processed sample and (d) SEM image of the UV LA and VIS LA processed sample.

2 pulses of UV & 2 pulses of UV plus VIS treatment

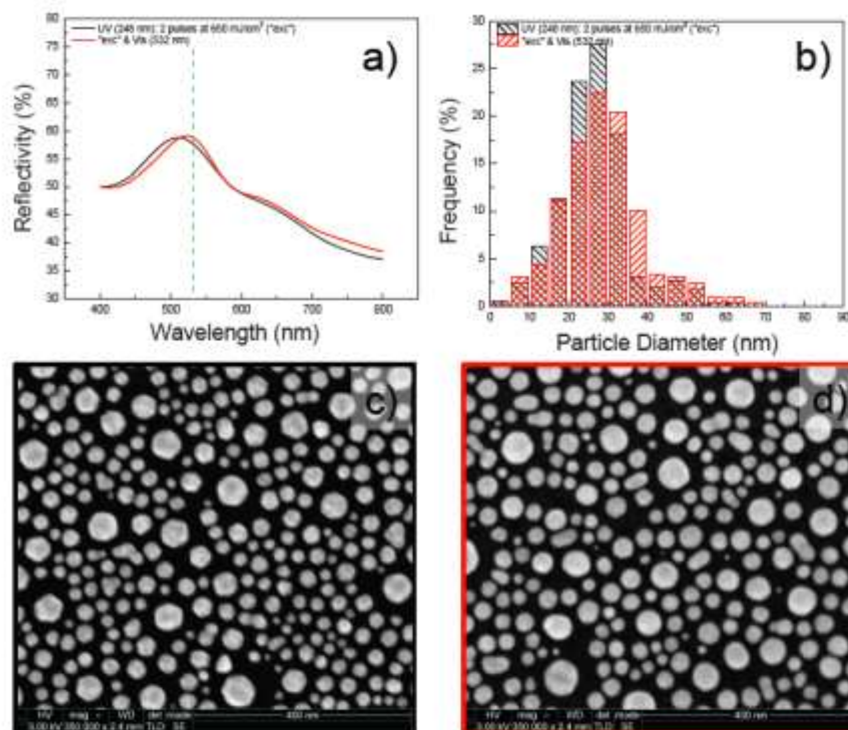

Figure S24. (a) ORS of the UV LA, 2 pulses at 650 mJ/cm^2 (black line), used as a template for the subsequent VIS LA process, 500 pulses at 125 mJ/cm^2 (red line). The green dashed line sets the 532 nm mark. (b) Particle size distributions derived from SEM imaging analysis of the sample processed with the UV LA (black shaded bars) and the sample treated with the UV LA and the VIS LA (red shaded bars), (c) SEM image of the UV LA processed sample and (d) SEM image of the UV LA and VIS LA processed sample.

3 pulses of UV & 3 pulses of UV plus VIS treatment

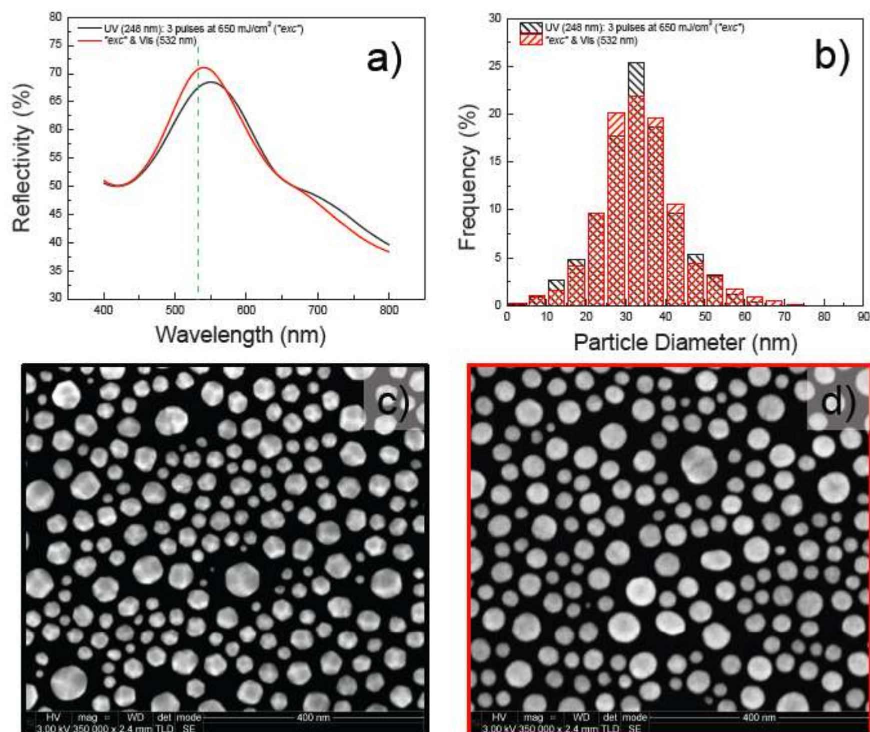

Figure S25. (a) ORS of the UV LA, 3 pulses at 650 mJ/cm^2 (black line), used as a template for the subsequent VIS LA process, 500 pulses at 125 mJ/cm^2 (red line). The green dashed line sets the 532 nm mark (b) Particle size distributions derived from SEM imaging analysis of the sample processed with the UV LA (black shaded bars) and the sample treated with the UV LA and the VIS LA (red shaded bars), (c) SEM image of the UV LA processed sample and (d) SEM image of the UV LA and VIS LA processed sample.

5 pulses of UV & 5 pulses of UV plus VIS treatment

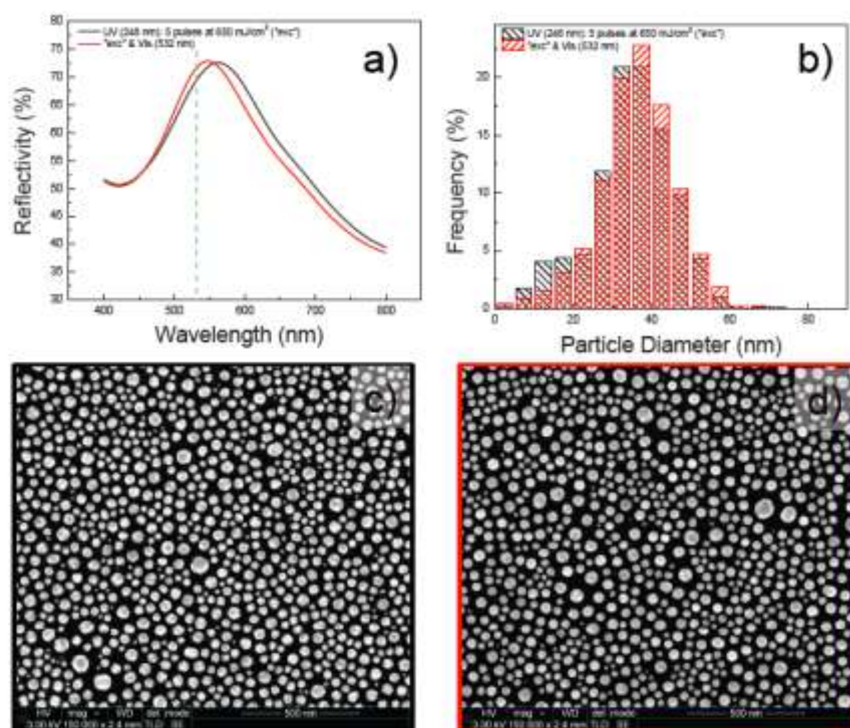

Figure S26. (a) ORS of the UV LA, 5 pulses at 650 mJ/cm^2 (black line), used as a template for the subsequent VIS LA process, 500 pulses at 125 mJ/cm^2 (red line). The green dashed line sets the 532 nm mark (b) Particle size distributions derived from SEM imaging analysis of the sample processed with the UV LA (black shaded bars) and the sample treated with the UV LA and the VIS LA (red shaded bars), (c) SEM image of the UV LA processed sample and (d) SEM image of the UV LA and VIS LA processed sample.

10 pulses of UV & 10 pulses of UV plus VIS treatment

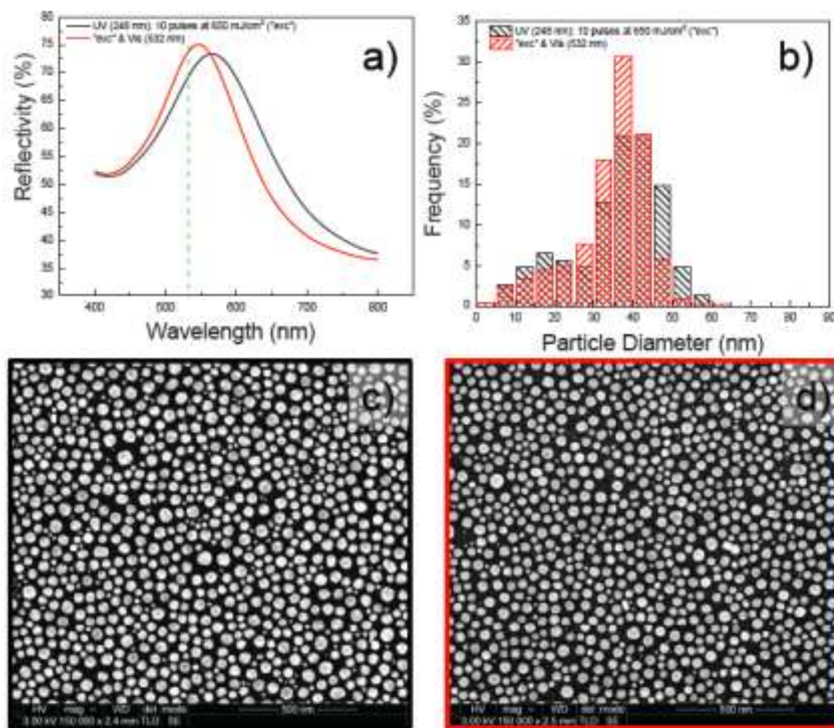

Figure S27. (a) ORS of the UV LA, 10 pulses at 650 mJ/cm^2 (black line), used as a template for the subsequent VIS LA process, 500 pulses at 125 mJ/cm^2 (red line). The green dashed line sets the 532 nm mark. (b) Particle size distributions derived from SEM imaging analysis of the sample processed with the UV LA (black shaded bars) and the sample treated with the UV LA and the VIS LA (red shaded bars), (c) SEM image of the UV LA processed sample and (d) SEM image of the UV LA and VIS LA processed sample.

15 pulses of UV & 15 pulses of UV plus VIS treatment

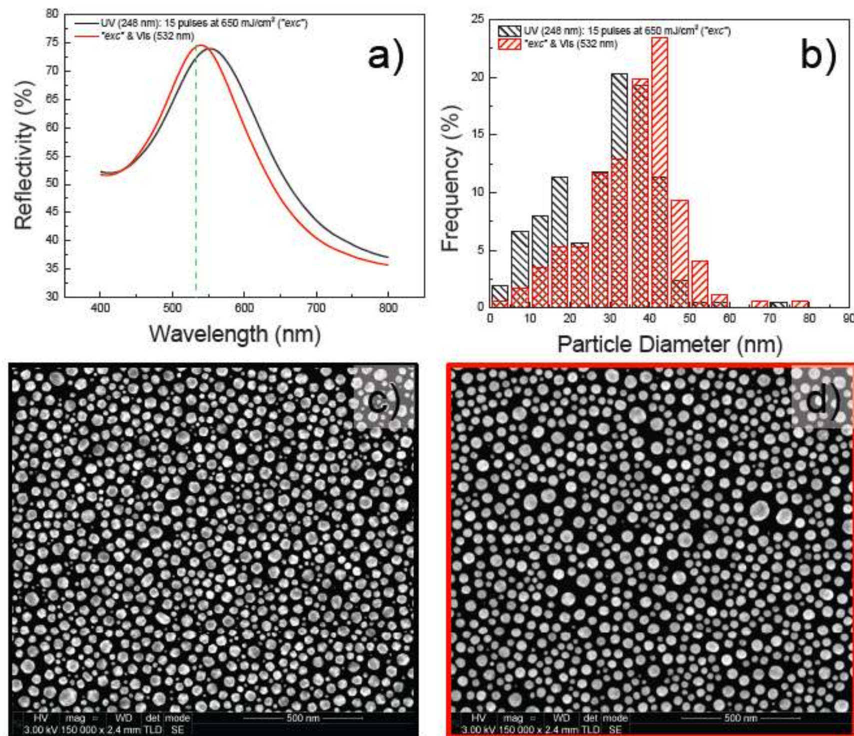

Figure S28. (a) ORS of the UV LA, 15 pulses at 650 mJ/cm^2 (black line), used as a template for the subsequent VIS LA process, 500 pulses at 125 mJ/cm^2 (red line). The green dashed line sets the 532 nm mark. (b) Particle size distributions derived from SEM imaging analysis of the sample processed with the UV LA (black shaded bars) and the sample treated with the UV LA and the VIS LA (red shaded bars), (c) SEM image of the UV LA processed sample and (d) SEM image of the UV LA and VIS LA processed sample.

LISA / UV *MONA-LISA* (248 nm, 800 mJ/cm^2)

1 pulse of UV & 1 pulse of UV plus VIS treatment

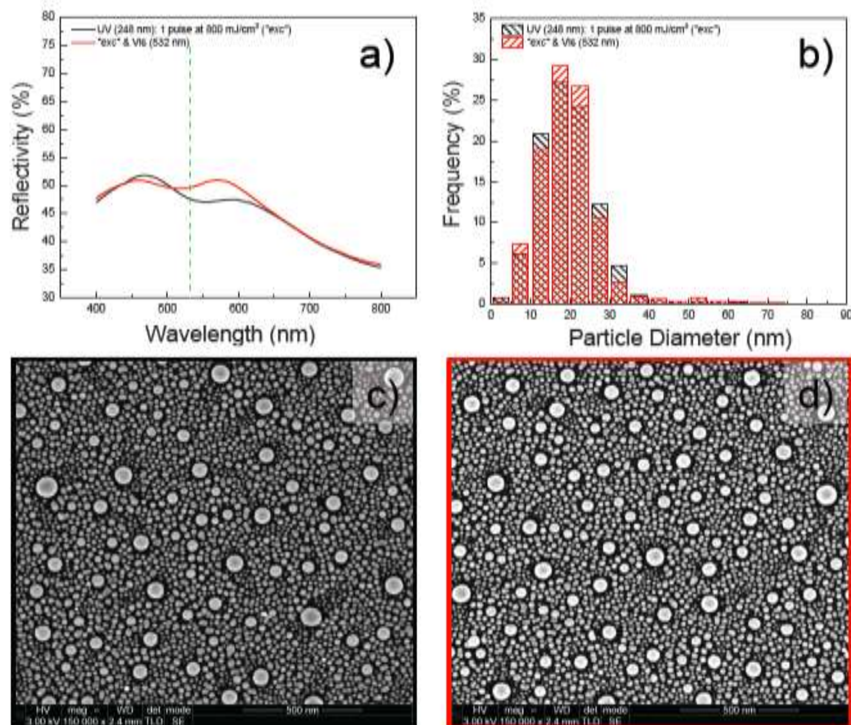

Figure S29. (a) ORS of the UV LA, 1 pulse at 800 mJ/cm^2 (black line), used as a template for the subsequent VIS LA process, 500 pulses at 125 mJ/cm^2 (red line). The green dashed line sets the 532 nm mark. (b) Particle size distributions derived from SEM imaging analysis of the sample processed with the UV LA (black shaded bars) and the sample treated with the UV LA and the VIS LA (red shaded bars), (c) SEM image of the UV LA processed sample and (d) SEM image of the UV LA and VIS LA processed sample.

2 pulses of UV & 2 pulses of UV plus VIS treatment

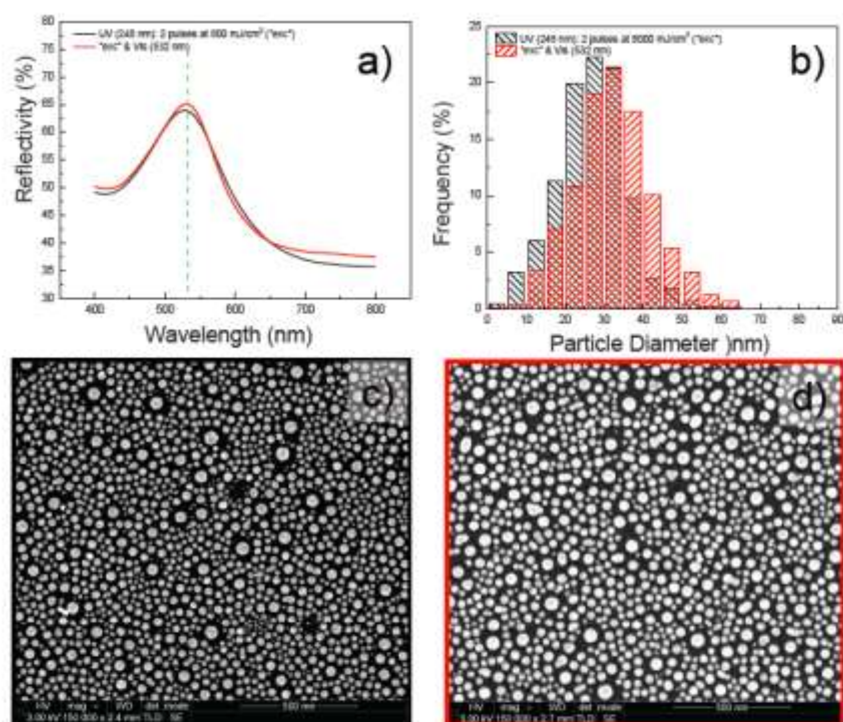

Figure S30. (a) ORS of the UV LA, 2 pulses at 800 mJ/cm^2 (black line), used as a template for the subsequent VIS LA process, 500 pulses at 125 mJ/cm^2 (red line). The green dashed line sets the 532 nm mark. (b) Particle size distributions derived from SEM imaging analysis of the sample processed with the UV LA (black shaded bars) and the sample treated with the UV LA and the VIS LA (red shaded bars), (c) SEM image of the UV LA processed sample and (d) SEM image of the UV LA and VIS LA processed sample.

3 pulses of UV & 3 pulses of UV plus VIS treatment

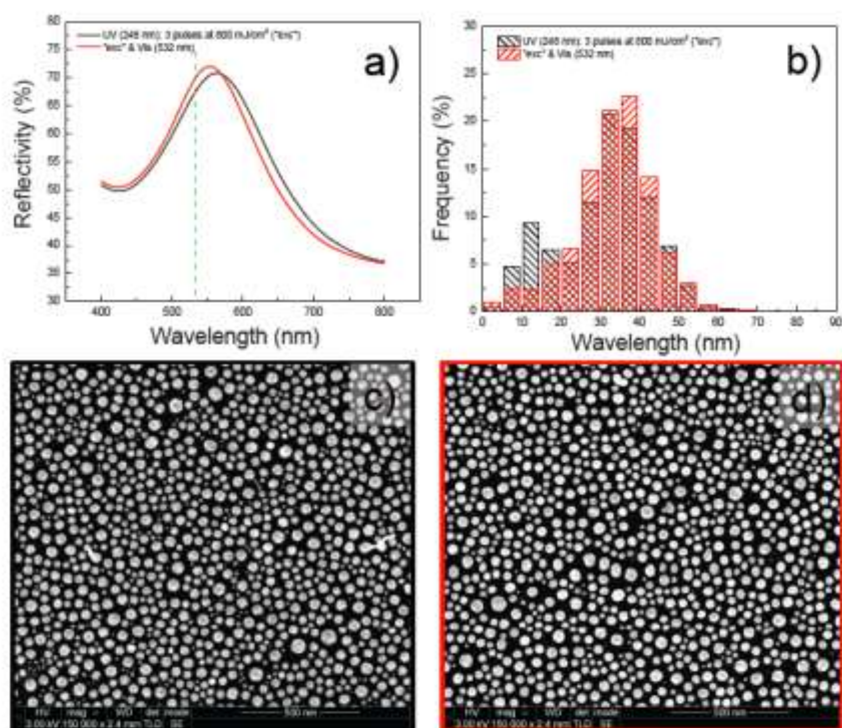

Figure S31. (a) ORS of the UV LA, 3 pulses at 800 mJ/cm^2 (black line), used as a template for the subsequent VIS LA process, 500 pulses at 125 mJ/cm^2 (red line). The green dashed line sets the 532 nm mark. (b) Particle size distributions derived from SEM imaging analysis of the sample processed with the UV LA (black shaded bars) and the sample treated with the UV LA and the VIS LA (red shaded bars), (c) SEM image of the UV LA processed sample and (d) SEM image of the UV LA and VIS LA processed sample.

5 pulses of UV & 5 pulses of UV plus VIS treatment

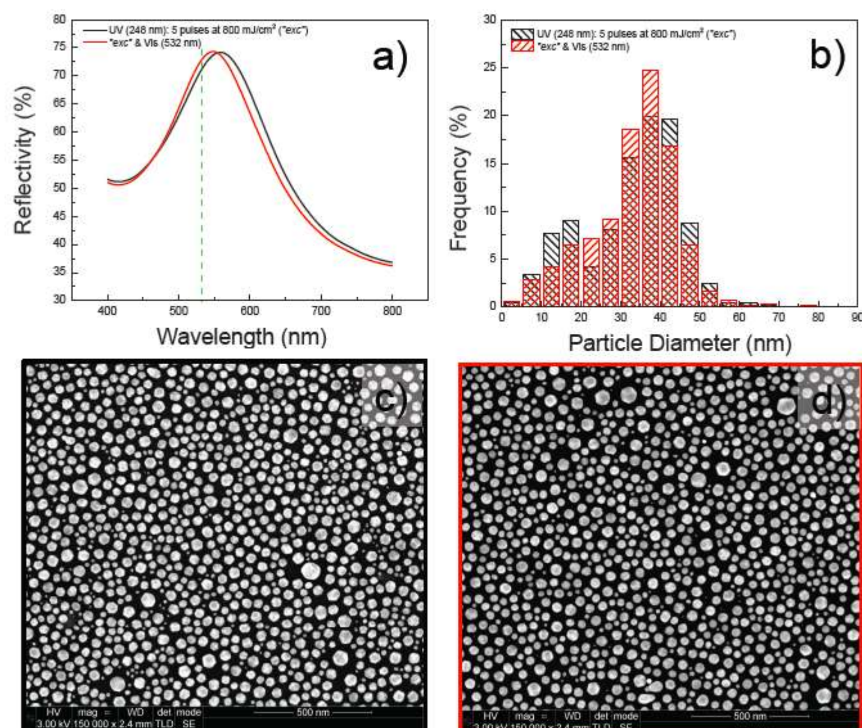

Figure S32. (a) ORS of the UV LA, 5 pulses at 800 mJ/cm^2 (black line), used as a template for the subsequent VIS LA process, 500 pulses at 125 mJ/cm^2 (red line). The green dashed line sets the 532 nm mark. (b) Particle size distributions derived from SEM imaging analysis of the sample processed with the UV LA (black shaded bars) and the sample treated with the UV LA and the VIS LA (red shaded bars), (c) SEM image of the UV LA processed sample and (d) SEM image of the UV LA and VIS LA processed sample.

10 pulses of UV & 10 pulses of UV plus VIS treatment

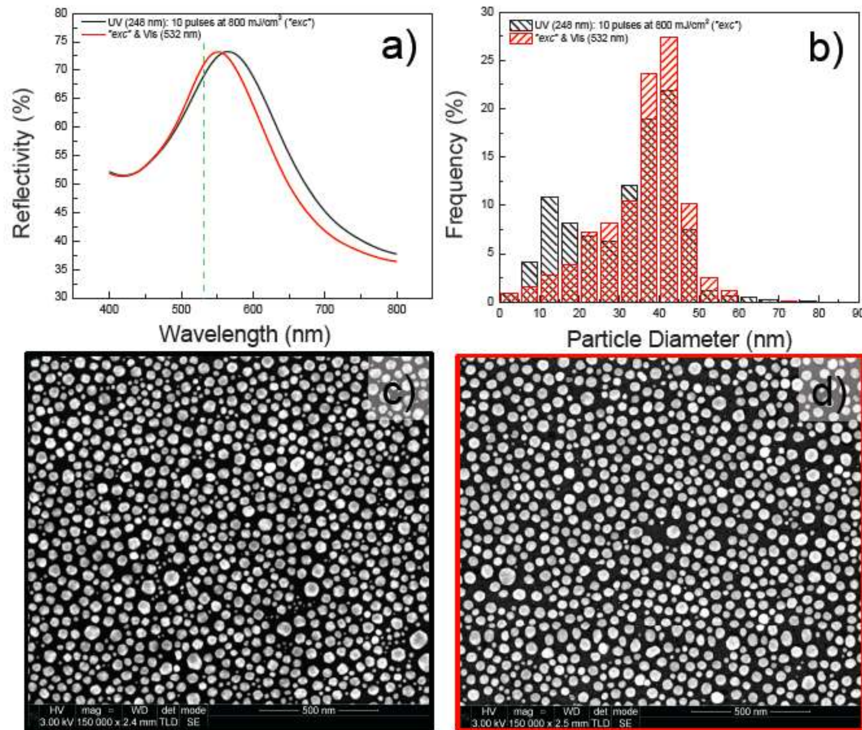

Figure S33. (a) ORS of the UV LA, 10 pulses at 800 mJ/cm^2 (black line), used as a template for the subsequent VIS LA process, 500 pulses at 125 mJ/cm^2 (red line). The green dashed line sets the 532 nm mark. (b) Particle size distributions derived from SEM imaging analysis of the sample processed with the UV LA (black shaded bars) and the sample treated with the UV LA and the VIS LA (red shaded bars), (c) SEM image of the UV LA processed sample and (d) SEM image of the UV LA and VIS LA processed sample.

15 pulses of UV & 15 pulses of UV plus VIS treatment

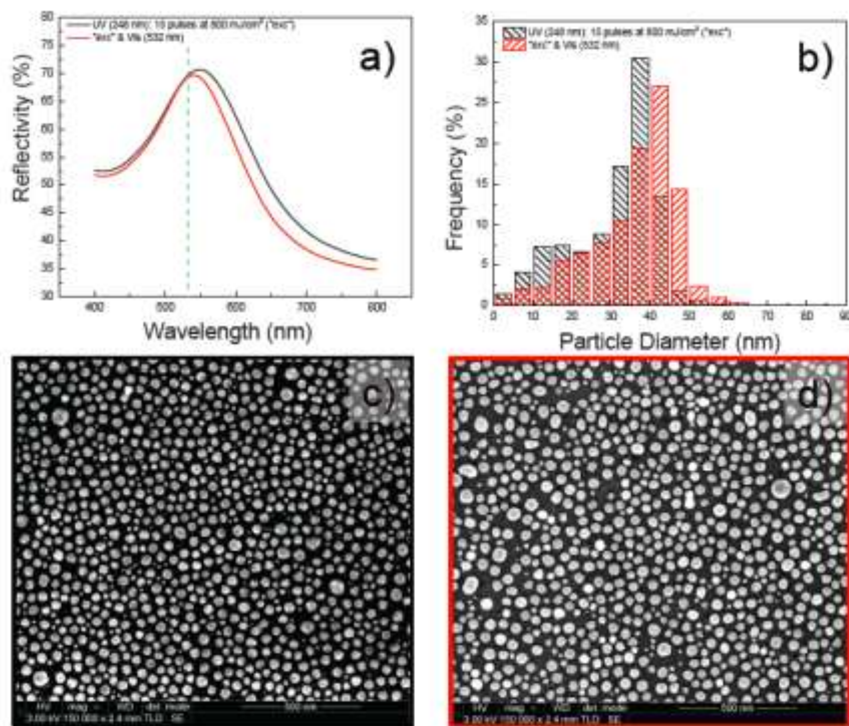

Figure S34. (a) ORS of the UV LA, 15 pulses at 800 mJ/cm^2 (black line), used as a template for the subsequent VIS LA process, 500 pulses at 125 mJ/cm^2 (red line). The green dashed line sets the 532 nm mark. (b) Particle size distributions derived from SEM imaging analysis of the sample processed with the UV LA (black shaded bars) and the sample treated with the UV LA and the VIS LA (red shaded bars), (c) SEM image of the UV LA processed sample and (d) SEM image of the UV LA and VIS LA processed sample.

ii. Ag thin films deposited by alternative techniques

A Ag thin film, 10 nm of effective thickness, was deposited be e-beam evaporation (EBE) to assess the generic approach of the *MONA-LISA* process. Two initial UV LA conditions were chosen as templates to be subsequently used for the VIS LA; 15 pulses at 500 mJ/cm^2 and 5 pulses at 800 mJ/cm^2. Both templates were then exposed to VIS LA (532 nm) for 500 pulses at 125 mJ/cm^2. The result of *MONA-LISA* is confirmed.

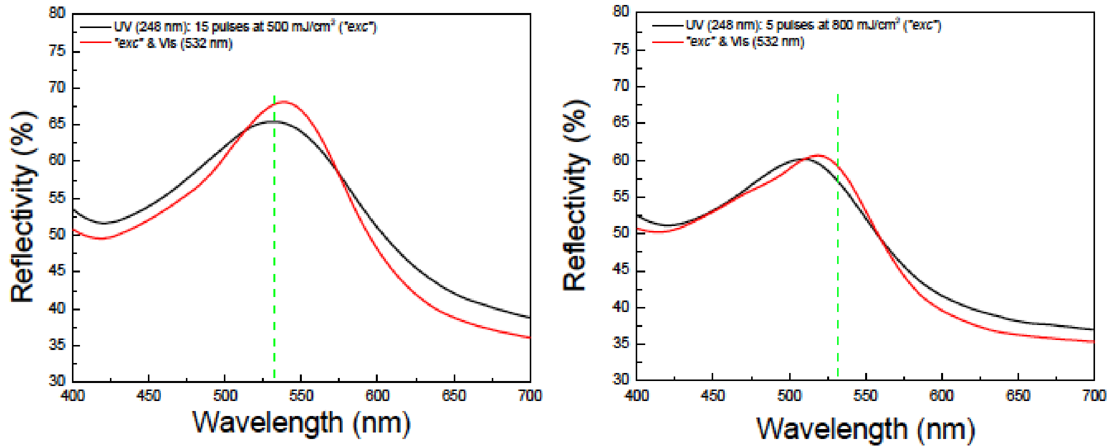

Figure S35. ORS of a Ag (10 nm) thin film fabricated by EBE of (a) UV LA, 15 pulses at 500 mJ/cm^2 (black line), used as a template for the subsequent VIS LA process, 500 pulses at 125 mJ/cm^2 (red line) and (b) UV LA, 5 pulses at 800 mJ/cm^2 (black line), used as a template for the subsequent VIS LA process, 500 pulses at 125 mJ/cm^2 (red line).

Additionally, we used a further alternative method; that of Ag deposition by chemical reduction of AgNO3 on commercial n-type Si (100) wafers by drop casting of an AgNO3/HF aqueous solution. In this case the chemical reduction produces nanoparticles, hence the UV LA is not required. VIS LA is applied only.

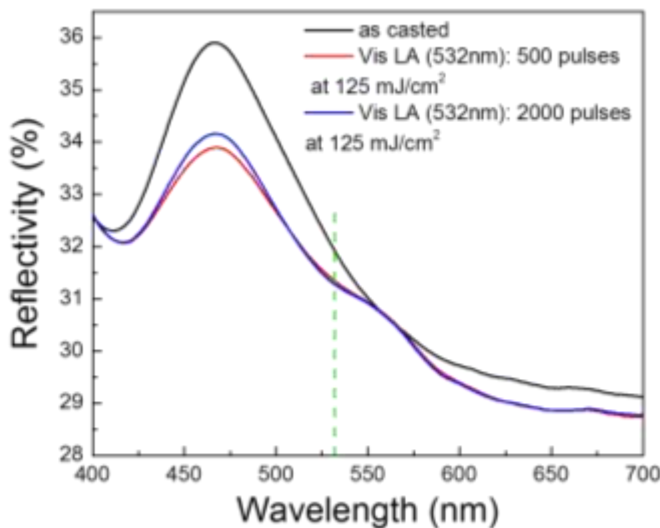

Figure S36. ORS of a Ag nanoparticles deposited by chemical reduction of AgNO3 on to Si wafers by drop casting (black line) and subsequently processed with VIS LA (532 nm), 500 pulses at 125 mJ/cm^2 (red line) and 2000 pulses at 125 mJ/cm^2 (blue line). Again the result of *MONA-LISA* is confirmed.

2.2 Combined irradiations of UV (248 nm) and VIS (532 nm) on Au thin films

The VIS *MONA-LISA* process has also been tested for Au thin films (shown on Fig. S37). An initial UV process of 15 pulses at 500 mJ/cm^2 was followed by a VIS irradiation of 500 pulses at 125 mJ/cm^2. The results of *MONA-LISA* process are confirmed by the narrower and higher reflectivity observed after the VIS LA, for the case of Au, as well. The inset figure presents the LSPR peaks after background subtraction. The corresponding values for the FWHM are also shown in the inset for comparison.

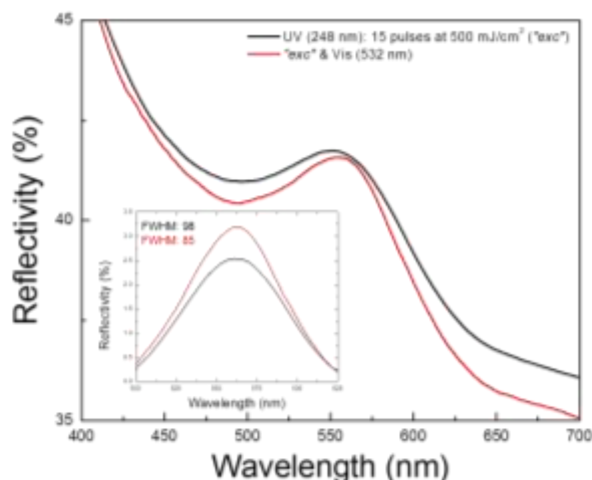

Figure S37. ORS of Au 5nm thin film fabricated by magnetron sputtering processed with UV LA, 15 pulses at 500 mJ/cm^2 (black line), used as a template for the subsequent VIS LA process, 500 pulses at 125 mJ/cm^2 (red line).

2.3 Combined irradiations of UV (248 nm) and VIS (620 nm) on Ag thin films

The *MONA-LISA* process has been, finally tested with a second VIS wavelength (620 nm). For this particular reason, a Ag thin film (10 nm), initially processed at UV LA (248 nm, 2 pulses at 350 mJ/cm^2), was subsequently processed with VIS LA (620 nm, from OPO) with 100 and 200 pulses at 120 mJ/cm^2. As shown in Fig. S38 below, a shift towards the processing wavelength and a narrower bandwidth is observed, similar to the case of the 532 nm VIS LA, thus proving the general concept of VIS MONA LISA.

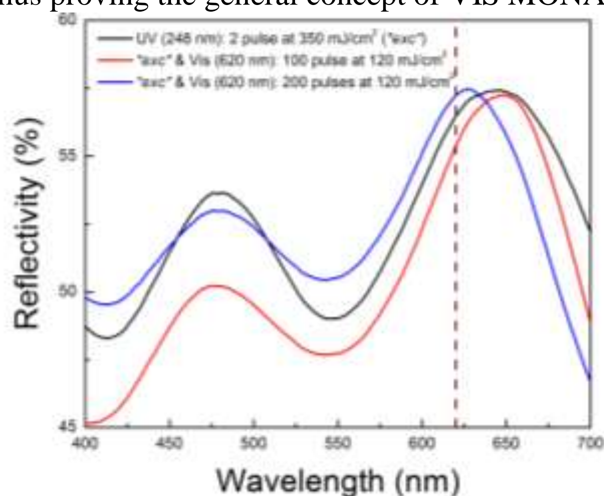

Figure S38. ORS of a Ag (10 nm) thin film fabricated by magnetron sputtering and UV LA, 2 pulses at 350 mJ/cm^2 (black line), used as a template for the subsequent VIS LA process, 100 pulses at 120 mJ/cm^2 (red line) and 200 pulses at 120 mJ/cm^2 (blue line). The dark red dashed

line sets the 620 nm mark. The effect of *MONA-LISA* is confirmed again by shifting the main resonance band towards the processing wavelength.

3. Reproducibility tests

Fig. S39 presents statistical analysis of the LSPR spectral position and LSPR reflectivity percentage for 30 samples produced by identical UV laser annealing conditions on the same Ag (10 nm) coated Si(100) wafer.

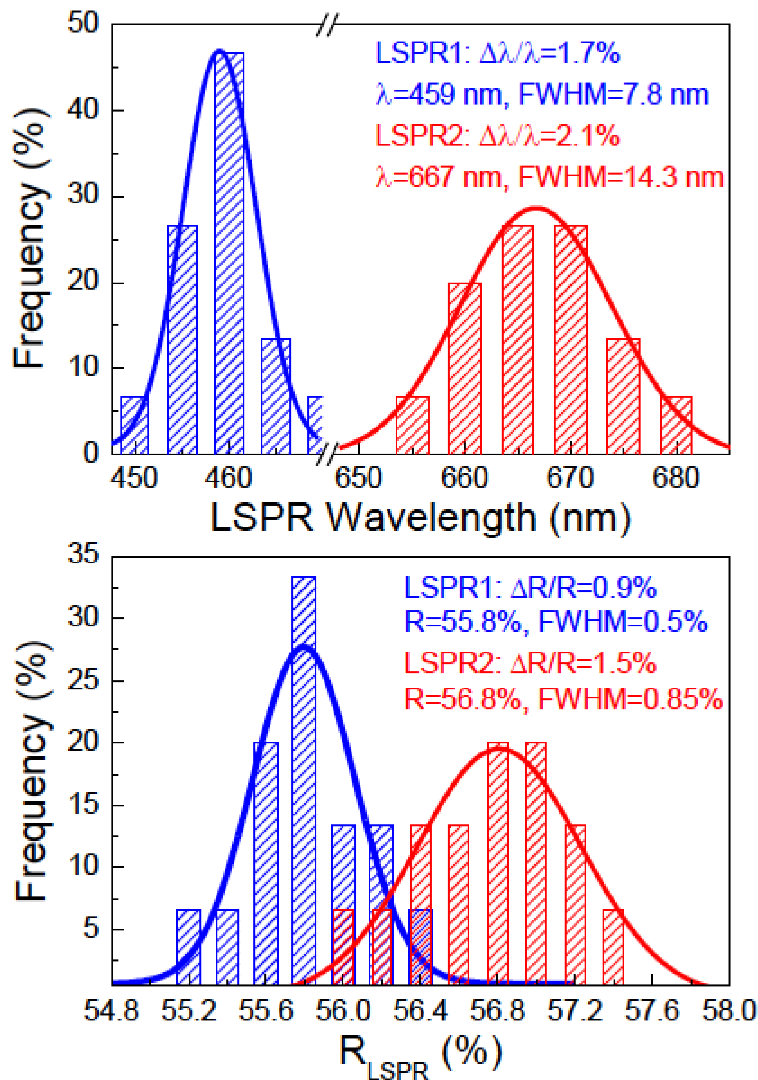

Figure S39. Reproducibility tests regarding the spectral position and reflectivity percentage of LSPR from 30 plasmonic templates produced by UV *MONA-LISA*.

4. Microscopy evaluation

Considering that the high-energy beam used in the SEM experiments (3 keV) could have an impact on the samples' morphology, we present results from an alternative microscopy technique, namely Atomic Force Microscopy (AFM). The AFM measurements were performed with a Dimension FastScan Scanning Probe Microscope (BRUKER). The AFM was placed on an anti-vibrational air stable granite stage housed inside an acoustic enclosure. Tapping mode was utilized for better image acquisition using extra sharp rectangular silicon cantilevers (nominal tip radius: 8 nm), with a constant force of 40 N/m.

Fig. S40c presents results of particle size distributions of the same sample (248 nm UV LA processing: 15 pulses at 650 mJ/cm^2) derived from AFM (Fig. S40a) and SEM (Fig. S40b). The red bars represent the results of the analysis on the SEM image, whereas the black bars represent the results of the analysis on the AFM image. Clearly, a good agreement between the two experimental techniques is observed and therefore we can be confident that the SEM is not altering ("destroying" or "creating") the morphology of the nanoparticles as created by the LA processes. In addition to that, we present in Fig. S40d a SEM image captured immediately after zooming out of the area of interest, where it is also clearly shown that the particle sizes within the darker box are identical to those in the surrounding areas. All these results suggest that the produced nanoparticle arrays are not harmed by either the mechanical forces applied by the AFM tip during measurement, neither by the high energy electron beam used in SEM.

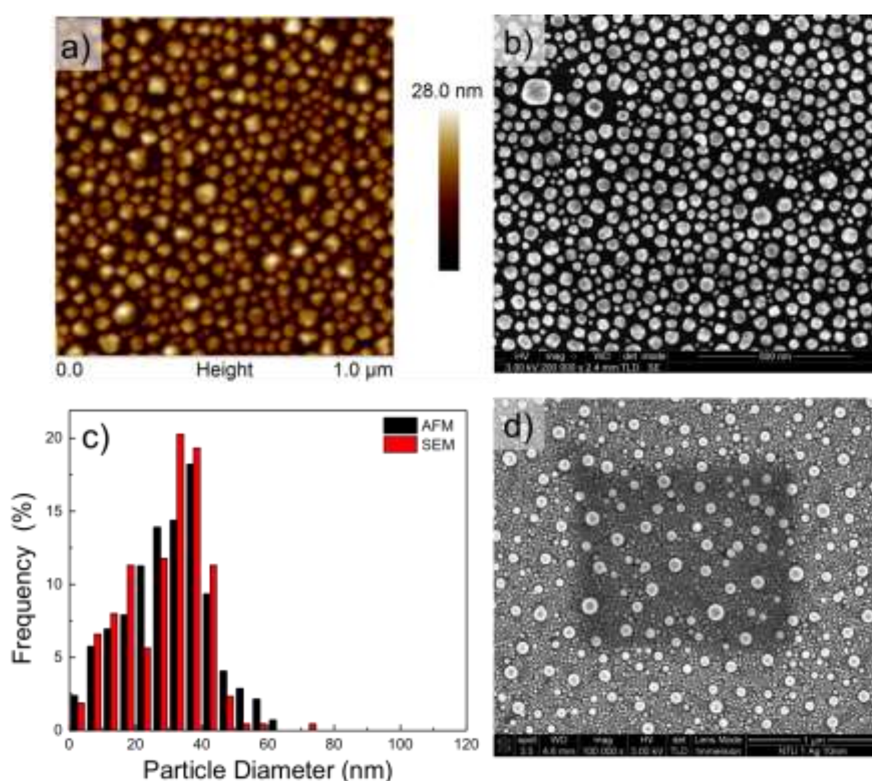

Figure S40. (a) AFM image of sample processed with a 248 nm UV LA (15 pulses at 650 mJ/cm^2), (b) SEM image of the same sample, (c) particle size distributions from AFM imaging (black bars) and SEM imaging (red bars) showing good agreement between the two experimental characterisation techniques, (d) SEM image captured immediately after zooming out from the area of interest showing that SEM does not alter the samples' surface morphology.

5. Details of the Excimer Laser Annealing experimental set up

UV Laser Annealing (LA) was carried out with an Excimer laser (LAMBDA PHYSIK LPX 305i) which is capable of delivering unpolarized light (pulse length of 25ns) and up to 1200 mJ/pulse at 248nm (KrF) or up to 600mJ/pulse at 193 nm (ArF). The raw beam is approximately 30mm x 15mm with a Gaussian like profile on the long axis and an almost top-hat profile on the short axis. The beam delivery system consists of a variable attenuator, a beam homogeniser and a mask-projection system. The variable attenuator employs a partially reflective first plate that can be angled, at various positions, reflecting more or less of the laser beam and a second plate that compensates for the parallel displacement of the beam caused by the first plate. The attenuator has a variable throughput from 0% up to 90% of the original beam. The beam homogenizer (Exitech Ltd., type EX-HS-700D) employs a pair of cylindrical lenses that expand the short axis of the beam to match the entrance aperture of the lens arrays to follow. The lens arrays consist of 64 separately closed pack spherical lenses mounted tightly together. The first array segments the input beam into 64 separate beamlets, each of which is focused and then re-expanded to intercept its corresponding lenslet of the second array. A condenser lens is placed immediately after the second lens array in order to intersect all the beamlets on the optical axis at the homogenizer output plane. As a result each beamlet is expanded and caused to overlap at the homogenizer output plane, providing a laser spot of predetermined size (13 mm x 13 mm), at a predetermined distance from the condenser lens and with top-hat profiles on both axes (better than 2% uniformity). This homogenized beam was arranged to coincide with a mask, which was then projected onto the sample via a combination of a field lens and a projection lens. A X-Y-Z stage was used in order to manipulate the sample and laser process different areas on it. The laser spot delivered onto the samples was set, by an appropriate mask and projection lenses, to be a 2.5×2.5 mm^2 spot.

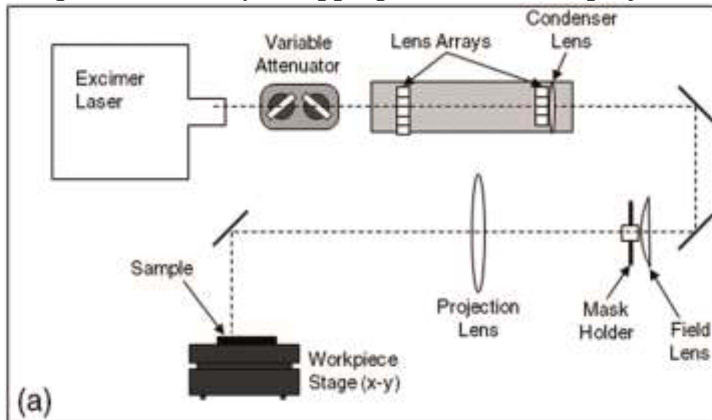

Figure S41. Schematic of the excimer laser annealing apparatus and optics.